UNIVERSITAT POLITÈCNICA DE CATALUNYA
BARCELONATECH
Escola d'Enginyeria de Barcelona Est

FINAL BACHELOR'S PROJECT

Materials engineering degree

3D PRINTING OF SOLID OXIDE FUEL CELLS

Report and Annexes

Author: Laura Cabezas i Peñalva
Director: Joan Josep Roa Rovira
Call for proposal: June 2018

Abstract

Nowadays, 3D printing is booming as a processing technique, thanks to its versatility in the manufacture of complex geometries and with a quality finish, which cannot be obtained using traditional techniques and can reduce the costs of table-processing (such as, for example, surface finishing, etc.). With this technology, the aim is to bring science and society closer together, with the ultimate goal of developing new devices that are much more efficient than the current ones in order to produce clean energy. Specifically, in the field of energy and in particular in 3D printing of solid oxide fuel cells, since the fuel used is derived from hydrogen in contact with air to produce energy and water vapour. Therefore, this technology avoids the generation of greenhouse gases, such as CO2.

The purpose of this final Bachelor's project (TFG) is the combination of these two fields, focusing on the electrolyte printing of solid oxide fuel cells, with the main objective of obtaining the final material with microstructural and mechanical properties similar to those obtained by traditional techniques. Nevertheless, through this Bachelor's project, a new research field will be implemented within the CIEFMA group (Centre for Structural Integrity and Reliability of Materials) of the Department of Materials Science and Metallurgic Engineering UPC's , with the future long term purpose of getting all the parts of the battery printed; electrolyte, cathode and anode.

To carry out this study, two geometries have been chosen, tubular and hexagonal, where the proportions of the printing material, processing conditions, etc. have been modified in order to achieve materials with a relative density higher than 99% and mechanical properties similar to the theoretical values of the materials used, by means of technical characterization advances (for example: electron microscopy, nanoindentació, etc.). Subsequently, the cathode was deposited by dip-coating and adhesion was studied by means of nanometric scale scratch-out tests.

A density greater than 99% has been obtained with a hardness and modulus of elasticity of the printed material comparable to the theoretical value obtained by conventional forming techniques. The cathode also has good adhesion to the electrolyte, since no cracks or other mechanisms of damage to the interface can be observed through the optical microscope

Resum

Actualment la impressió 3D esta tenint un fort auge com a tècnica de processat, gràcies a la seva versatilitat en la fabricació de geometries complexes i amb un acabat de qualitat, les quals no és poden obtenir mitjançant les tècniques tradicionals i permeten reduir costos de post-processat (com per exemple, acabat superficial, etc.). Amb aquesta tecnologia, s'intenta aproximar la ciència amb la societat, amb l'objectiu final de desenvolupar nous dispositius molt més eficients que els actuals per produir energia neta. Concretament, en el camp de l'energia i en particular en la impressió 3D de piles de combustible d'òxid sòlid, ja que el combustible que s'utilitza són derivats de l'hidrogen amb contacte en l'aire per tal de produir energia i vapor d'aigua. Per tant, mitjançant aquesta tecnologia, s'evita la generació de gasos d'efecte hivernacle, com el CO_2.

El propòsit d'aquest treball final de grau (TFG) és la combinació d'aquests dos camps, centrant-se en la impressió del electròlit de les piles de combustible d'òxid sòlid, amb l'objectiu principal d'obtenir els material final amb unes propietats microestructurals i mecàniques semblant a les obtingudes per les tècniques tradicionals. Tanmateix, mitjançant aquest TFG s'intentarà implementar un nou camp d'investigació dins del grup CIEFMA (Centre d'Integritat Estructural i Fiabilitat dels Materials) del departament de Ciència dels Materials i Eng. Metal·lúrgica de la UPC, amb el futur propòsit a llarg plaç d'aconseguir imprimir totes les parts de la pila; electròlit, càtode i ànode.

Per dur a terme aquest estudi dues geometries s'han triat, tubular i hexagonal, on s'han anat modificant les proporcions del material d'impressió, condicions de processat, etc, per poder assolir materials amb una densitat relativa superior al 99% i propietats mecàniques similars als valors teòrics dels materials emprats, mitjançant tècniques avançades de caracterització (per exemple: microscopia electrònica, nanoindentació, etc.). Posteriorment, s'ha dipositat el càtode mitjançant el "dip-coating" i s'ha estudiat l'adhesió mitjançant assajos de ratllat a escala nanomètrica.

S'ha obtingut una densitat superior al 99% amb una duresa i mòdul d'elasticitat del material imprès comparable al valor teòric obtingut per tècniques convencionals de conformat. Tan mateix, el càtode presenta una bona adherència amb l'electròlit, ja que mitjançant el microscopi òptic no s'observen esquerdes ni altres mecanismes de dany a la interfase.

Resumen

Actualmente la impresión 3D está teniendo un fuerte auge como técnica de procesado, gracias a su versatilidad en la fabricación de geometrías complejas y con un acabado de calidad, las cuales no es pueden obtener mediante las técnicas tradicionales y permiten reducir costes de tabla-procesado (cómo por ejemplo, acabado superficial, etc.). Con esta tecnología, se intenta aproximar la ciencia con la sociedad, con el objetivo final de desarrollar nuevos dispositivos mucho más eficientes que los actuales para producir energía limpia. Concretamente, en el campo de la energía y en particular en la impresión 3D de pilas de combustible de óxido sólido, puesto que el combustible que se utiliza son derivados del hidrógeno con contacto en el aire para producir energía y vapor de agua. Por lo tanto, mediante esta tecnología, se evita la generación de gases de efecto invernadero, como el CO2.

El propósito de este trabajo final de grado (TFG) es la combinación de estos dos campos, centrándose en la impresión del electrólito de las pilas de combustible de óxido sólido, con el objetivo principal de obtener los materiales finales con unas propiedades microestructurals y mecánicas parecidas a las obtenidas por las técnicas tradicionales. Aun así, mediante este TFG se intentará implementar un nuevo campo de investigación dentro del grupo CIEFMA (Centro de Integridad Estructural y Fiabilidad de los Materiales) del departamento de Ciencia de los Materiales y Ing. Metalúrgica de la UPC, con el futuro propósito a largo plaç de conseguir imprimir todas las partes de la pila; electrólito, cátodo y ánodo.

Para llevar a cabo este estudio dos geometrías se han elegido, tubular y hexagonal, donde se han ido modificando las proporciones del material de impresión, condiciones de procesado, etc., para poder lograr materiales con una densidad relativa superior al 99% y propiedades mecánicas similares a los valores teóricos de los materiales empleados, mediante técnicos avances de caracterización (por ejemplo: microscopia electrónica, nanoindentació, etc.). Posteriormente, se ha depositado el cátodo mediante el “dip-coating” y se ha estudiado la adhesión mediante ensayos de tachado a escala nanomètrica.

Se ha obtenido una densidad superior al 99% con una dureza y módulo de elasticidad del material imprimido comparable al valor teórico obtenido por técnicas convencionales de conformado. Tan mismo, el cátodo presenta una buena adherencia con el electrólito, puesto que mediante el microscopio óptico no se observan grietas ni otros mecanismos de daño a la interfase.

Acknowledgements

The work presented in this final bachelor's project would not have been possible to accomplish without guidance, motivation, help and knowledge of many people.

First of all I would like to express generous gratitude to my supervisor Joan Josep Roa, to give me the chance to start to work with him on this topic, and having full confidence in myself and my work. I would like to acknowledge to two PhD students, Hossein Besharatloo to give me a huge help with the nanoindentation part, and Joaquim Minguela that give to me disinterested assistance during the two month that my supervisor was working out of Spain.

I would like to acknowledge to my work mates during these months that we made a really nice work group and they give me moral support and assistance, and also to my friends for accompanying me on this long journey.

To finish, I am very thankful to my parents. They are my moral support not just during this project, and they always try to find the positive side of all the things.

Glossary of terms

AM: Additive manufacturing

SOFC: Solid oxide fuel cell

YSZ: Yttria-stabilised zirconia

XY-TZP: Tetragonal zirconia partial stabilized with x molar percentage of yttria

TT: Thermal treatment.

SLS: Selective laser sintering.

DLF: Direct laser fabrication.

LSM: Lanthanum gallate strontium and magnesium doped

OM: Optic microscope

AFM: Atomic force microscopy

SEM: Scanning electron microscopy

FIB: Focused ion beam

XRD: X-ray diffraction

H: Hardness

E: Elastic modulus

h: Displacement into surface

P: Applied load

K_{IC}: Fracture toughness

Motivation

Nowadays, the additive manufacturing (AM) is a worldwide methodology widely employed in many fields, e.g. energy, bioengineering, among others. Within this context, the AM methodology presents a growing trend due to it allows develop complex geometries with similar microstructural and mechanical properties for the specimens performed with the conventional processing techniques; e.g. cold and hot isostatic pressing (CIP and HIP, respectively), etc.

During the first semester of the present academic course (2017/2018) I was conducting a research stage during four months in the Structural Integrity, Micromechanics and Reliability of Materials research group (CIEFMA's group) at the Department of Materials Science and Metallurgical Engineering under the supervision of Dr. Joan Josep Roa Rovira. During this period, I was working in the following topic: "Microstructural and micromechanical correlation of zirconia based ceramic samples produced by Rapid Prototyping". As a consequence of this research stage different presentations were done around worldwide:

(1) ***Invited Seminar at "Saint-Gobain, Centre de Rescherches et d'etudes Europeen, Cavaillon Cedex (France)".*** *Corresponding author: Dr. Joan Josep Roa (December 2017).*
(2) ***Invited Seminar at "Universidad Católica Boliviana, Cochabamba (Bolívia)".*** *Corresponding author: Dr. Joan Josep Roa (March 2018).*
(3) ***Conference: Young Ceramists Additive Manufacturing Forum (University of Padova-Padova, Italy) (May 2018).*** *Corresponding author: Laura Cabezas*

Within this context, this Bachelor's project is the continuation of my previous work entitled: "*Study of mechanical properties of zirconia base ceramic materials applied in 3D printing"* using the AM methodology and in particular the 3D printing in order to develop two different solid oxide fuel cells (SOFCs) geometries (planar and tubular) in collaboration with IREC (Catalan Institute of Research of Energy), which is a centre that one of the groups are been working on SOFCs, and one of the lasts works was printing SOFCs. Within this Bachelor's project also we would like to establish long term collaboration between the CIEFMA's group and IREC.

The long term goal is to improve the performance of the SOFCs performed enhancing their final mechanical properties.

Table of contents

1. Introduction

1.1. Additive Manufacturing

Additive manufacturing (AM) are all manufacturing techniques based on obtaining the final part from a virtual 3D model by successive addition of material layer by layer until the desired geometry is reached; that is, the final geometry can be chosen arbitrarily without the need to modify the rest of the manufacturing process. This last fact gives rise to the appearance of a great number of opportunities within the scientific and industrial field, being considered one of the great revolutions of the 21st century.

1.1.1. Why Additive Manufacturing?

Apart from saving money and time, the following advantages are the main reasons why nowadays the AM is the most popular and suitable technique to design new materials in front of traditional techniques [1]:

1. A physical model that can be delivered quickly from CAD documents, can permit form, fit and function tests much prior in the design cycle.
2. Errors from incorrect interpretation of the design are reduced and designs to prototype iterations are faster.
3. It is possible to go from a CAD model to a prototype without using a skilled machinist, a fixture designer.
4. Core/Cavity can be built for plastic moulding, investment casting, and die-casting applications.
5. Apart from directly producing plastic prototype models, some of the parts produced can be used as patterns for investment or sand casting, depending on the technology used.
6. For producing dies and moulds longer lead-time is required. By AM technology, tooling can be produced in a shorter time, is needed a few hours to get the green body sample and after that perform the heat treatment in order to get a dense and mechanically resistant component. This helps in bringing the products to the market in a lesser time.
7. With appropriate materials, the model can be utilized as a part of consequent assembling operations to create the final parts. This also serves as a manufacturing technology.

1.1.2. Different production methodologies

As far as the AM of ceramic materials is concerned, there are many techniques depending on the morphology and final properties required for the desired pieces with a complex geometry. In general terms, they can be classified into three main groups based on the nature of the production process:

a) Manufacturing additive by negative

This set includes all those techniques based on obtaining a sacrificial polymeric mould by means of AM in which a ceramic paste is introduced. The whole is subjected to a thermal treatment (T.T.) by which the decomposition of the polymer mould and sintering of the ceramic piece is caused.

The lines of study using this type of technique are very diverse, for example, moulds obtained by laser sintering (L.S.) of epoxy resins have been widely employed to generate diamond structures of SiO_2/TiO_2 for photonic crystals application [2], or the obtaining of hydroxyapatite scaffolds with 50% porosity, as it is shown in ***figure 1.1***, for the replacement of bone tissue by means of the moulding of ceramic gels [3].

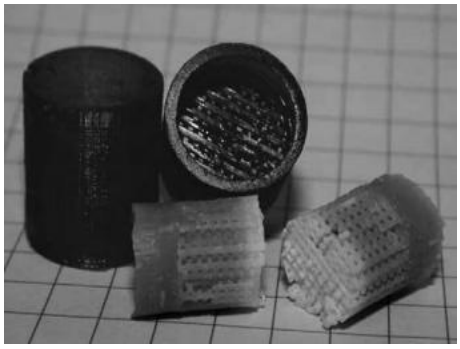

Figure 1.1: Resin casting moulds and sintered structures made of hydroxyapatite [3].

b) Indirect additive manufacturing

This category includes those manufacturing methods by which the final ceramic piece is obtained through successive addition of layers composed of ceramic material and vehicle or binder that require a post-processing treatment to develop a dense structure, an example is depicted in ***Figure 1.2.a***. Furthermore, inside of this manufacturing methodology, there different methods can be sub-classified:

i) Powder-based 3D printing: This method consists of the deposition of thin layers of ceramic powder on which a binding medium is impregnated, the nature of which may be aqueous or polymeric. Subsequently, the unit is subjected to a T.T. that sequentially removes the binding

medium by decomposition and sinters the powder to obtain the desired ceramic piece with the final geometry. This method yields pieces with high residual porosities, making it a technique quite suitable for the preparation of scaffolds in the field of tissue engineering, as it can be seen in ***Figure 1.2.b*** [4,5], although relatively high densities can be achieved by physically and chemically modifying the ceramic material to facilitate sintering [6,7].

ii) Powder-based selective L. S.: Its nature is virtually identical to that of 3D powder-based printing, although in this case powder densification is carried out by focusing a laser beam on the powder layers. The technique can be based on the direct sintering of ceramic powder (less common due to the poor mechanical properties) or on the melting of inorganic [8] or polymeric binders [9]. Again, the porosities obtained are high (near 30%), so it is not common to obtain monolithic parts, in addition to generating cracks by thermal shock. The main advantage of laser sintering is the greater geometrical precision that allows for more optimized structures to be obtained, making it extremely useful in the field of tissue engineering.

iii) Stereo lithography: This is based on the printing of a ceramic suspension on a liquid polymer resin, subsequent light-curing of the matrix and sintering T.T are required. Its main advantage over other indirect techniques is the possibility of obtaining practically dense structures due to the high concentration of ceramic material in the matrix.

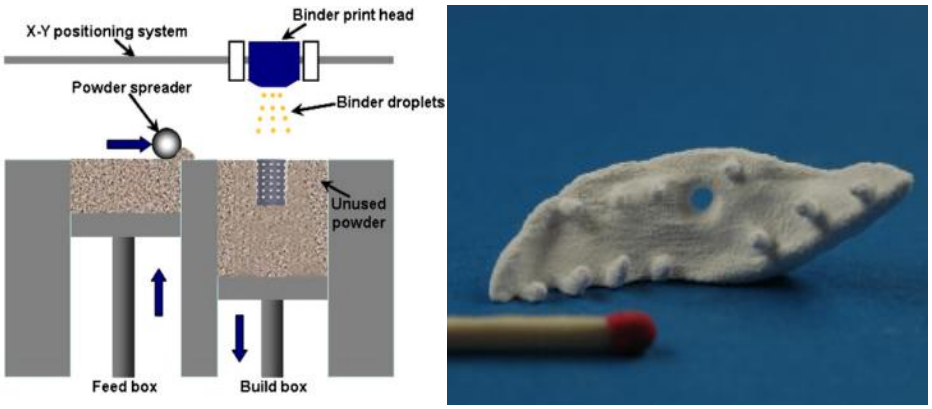

Figure 1.2: *(a) Schematic drawing representing the AM process [6]. (b) Printed structure of a model of an implant. The implant was printed with a commercial 3D printer using granulate consisting of TCP and BGH glass, two different types of bioceramic [4].*

c) Direct additive manufacturing

This group includes the techniques by means of which the final geometry is obtained directly from the printed ceramic material with a single stage of sintering heat treatment, without the need for intermediate treatments on the printing matrix. Two different sub-categories can be found:

i) Direct inkjet printing (InkJet): This is based on the spray deposition of liquid suspensions with a very high ceramic content (> 33% vol.). These suspensions contain different additives in order to regulate viscosity, surface tension and suspension power capacity, so that the ink properties can be adjusted to the printing system and the required final properties. In this way, complex geometries with a high degree of particle packing can be obtained which, through a careful sintering program, give rise to remarkable mechanical properties [10]. In addition, the minimum droplet size of the pico-litter order allows a great control over the distribution of the composition of the piece, being able to generate multimaterial structures [11].

Although this is a technique highly used in the development of 2D parts, the poor mechanical properties (e.g. hardness, fracture toughness, elastic modulus, etc.) of the printed specimens using these suspensions prevent their application in the development of 3D geometries.

ii) 3D Printing by filament extrusion (robocasting [12]): It consists of extruding through one or more heads of a viscous ceramic paste comprised of the ceramic powder charge and a suspension medium. The control of the rheological properties is a key parameter to prevent the deformation of the printed geometry, for which there are several methods such as controlled flocculation of the suspensions to obtain gels [13] (by modification of the pH or ionic strength of the solvent) or the addition of gelling additives [14].

Due to the high particle packing density achieved through the use of this technique, the mechanical properties of the parts obtained are generally greater than those of similar geometries and porosity obtained through other A.M. methods. However, the very nature of the process, consisting in the extrusion of independent yarns that make the structure a discontinuous fabric, as well as the matrix that must be eliminated during the T.T., which fully densify the material.

By using this methodology, porous bioceramic structures can be found in order to be used as scaffolds in the field of tissue engineering, an example of that is shown in ***Figure 1.3.*** The versatility of this technique leads to be used for a wide range of applications, for example: to obtain periodic networks of PZT (Lead Zirconate Titanate) with applications in ultrasonic detection [15], or the construction of ternary dielectric structures of ceramic perovskites structures (e.g. $BaTiO_3$, $BaZrO_3$ and $SrTiO_3$) by means of the use of three heads and a filament mixer [16].

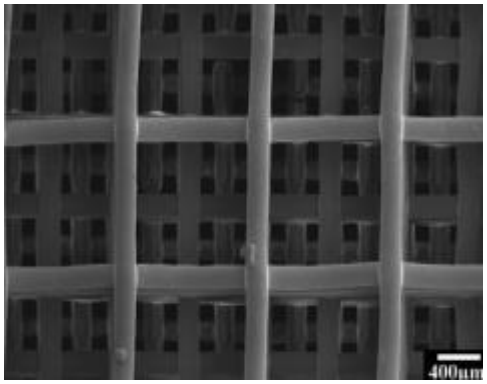

Figure 1.3: *An example of a pattern use for a glass scaffold with a gradient pore size [14].*

1.1.3. Advantages and disadvantages

One of the characteristics of the AM is the complex geometries that you can get. And another good thing is that this technique can be employed to print all kind of materials; ceramics, metals, polymers, even composites with multilayer of multimaterial systems. Apart of these characteristics, the following **advantages** can be found [1]:

1. Material efficiency: Unlike conventional subtractive manufacturing where large amount of materials need to be removed, AM uses raw materials efficiently by building parts layer by layer. Leftover materials can often be reused with minimum processing.
2. Resource efficiency: Conventional manufacturing processes require auxiliary resources such as jigs, fixtures, cutting tools, and coolants in addition to the main machine tool. AM does not require these additional resources. As a result, parts can be made by small manufacturers that are close to customers. This presents an opportunity for improved supply chain dynamics.
3. Part flexibility: Because there are no tooling constraints, parts with complex features can be made in a single piece. In other words, there is no need to sacrifice part functionality for the ease of manufacture. In addition, it is possible to build a single part with varying mechanical properties (flexible in one part and stiffer in another part). This opens up opportunities for design innovation in terms of microstructural and mechanical design only by designing complex microstructures.
4. Flexibility: AM machines do not require costly setups and hence is economical in small batch production. The quality of the parts depends on the process rather than operator skills. As such, production can be easily synchronized with customer demand. In addition, the problems of line balancing and production bottle-necks are virtually eliminated because complex parts are produced in single pieces

Despite this, AM technology still cannot fully competitive with the conventional manufacturing techniques, especially in the mass production field because of the following **drawbacks or disadvantages** [17]:

1. Size limitations: AM processes often use liquid polymers, or a powder comprised of resin or plaster, to build object layers. These materials render AM unable to produce large-sized objects due to lack of material strength. Large-sized objects also often are impractical due to the extended amount of time need to complete the build process.
2. Imperfections: Parts produced using AM processes often possess a rough and ribbed surface finish. This appearance is due to plastic beads or large-sized powder particles that are stacked on top of each other, giving the end product an unfinished look
3. Cost: AM equipment is considered an expensive investment. Entry level 3D printers average approximately 2,500€ and can go as high as 25,000€ for higher-end models, not including the cost of accessories and resins or other operational materials.

1.1.4. Applications

Due to all the advantages presented in ***section 1.1.3,*** this methodology can be apply on different fields with different requirements and final applications. Because you can modify the final piece with the modification of parameters like the porosity of your green sample, the addition of additives. Within this context, the AM technique has a wide range of applications, like:

- Biomedical: To fabricate orthopedic implants, as can be seen in ***Figure 1.4.a***. Furthermore in this sector, the tissue engineering field uses this methodology to fabricate 3D-scaffolds with different applications. Furthermore, this technology also will lead to generate medical devices like stems, among others.
- Aerospace: To fabricate complex components with rare geometries and are made usually from advanced materials (see ***Figure 1.4.b***), such as titanium alloys, nickel super alloys, special steels or ultra-high-temperature ceramics, which are difficult, costly and time-consuming to manufacture by using the conventional routes. Additionally, aerospace production is usually small, limited to a maximum of several thousand parts [1], allowing the AM a suitable technique to be employed in this field.
- Automotive: To fabricate new products. This process is critical for the automotive industry, due to it is often a very costly and time-consuming process. The automotive industry has been using AM technology as an important tool in the design and development of automotive components because it can shorten the development cycle and reduce manufacturing and product costs. AM processes also have been used to make small quantities of structural and functional parts, such as engine exhausts, drive shafts, gear box components and breaking systems for luxury, low volume vehicles. Unlike passenger cars,

vehicles for motorsports usually use light-weight alloys (e.g. titanium, etc.) and have highly complex structures and low production volumes. Companies and research institutes also have successfully applied AM techniques to manufacture functional components for racing vehicles. Even the AM can be applied to produce safety complements for the users of this high-technology in motorsports, and a good example of this is shown in the ***Figure 1.4.c.***

- Energy: This field has an important role on this project, because the technique of AM is a good way to generate complex fuel cells, like the solid oxide fuel cells (SOFCs) that is depicted in ***Figure 1.4.d,*** which is a good solution to reduce the dependence of fossil energy due to the fuel cells have a high efficiency, high power density and low emissions to the environment compared with the traditional energies. Furthermore, in this strategic field, the AM also leads to develop several components for catalytic applications, among others.

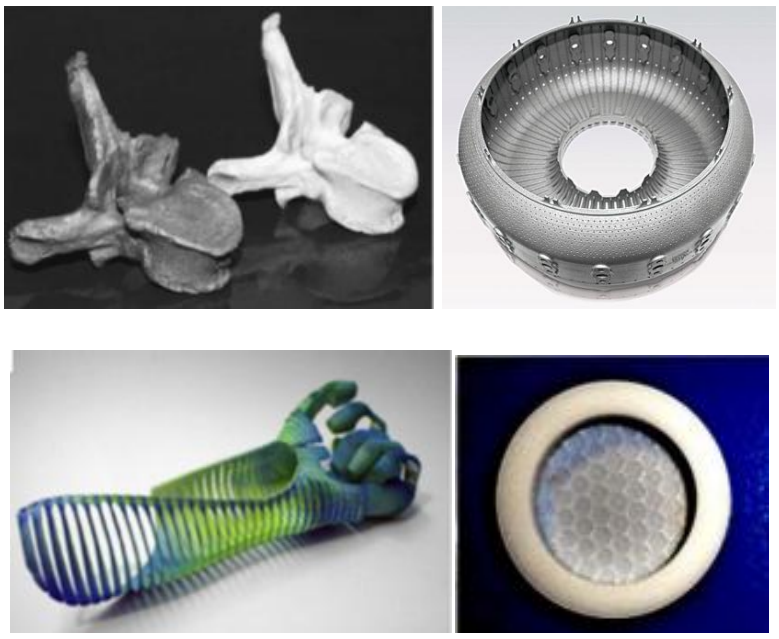

Figure 1.4*: (a) Replica of human vertebrae fabricated by AM and after that by SLS/DLF techniques [18], (b) Jet engine combustor of nickel alloy made with direct metal laser sintering [19], (c) 3D printed multi-material motorcycle "glove" [20] and (d) an electrolyte 3D printed of 3Y-TZP [21] .*

In this Bachelor's project, we will centre our attention to develop new devices to be employed in the energy field, concretely, we will focus our attention to develop new fuel cells; in particular, solid oxide fuel cells (SOFC) developed through the AM technology. More information about the Fuel Cells and in particular to the SOFC cells can be found in **section 1.2**

1.2. Fuel cells

This Bachelor's project is focused to develop 3D-SOFC produced by using the AM methodology. This kind of fuel cells usually are a base of ceramic fuel cells, because the electrolyte is an oxide of a metal which it means that it is a ceramic. This gives to the fuel cell the characteristic name, because the electrolyte is in the solid state form by a metal oxide. Furthermore, this type of fuels uses to work at intermediate temperature, ranged between 600 to 1000 ºC, which leads to promote a rapid reaction kinetics, giving a good performance. And also they give the elimination of the corrosion and the generation of unique designs giving improvements on mechanical properties.

But always there are some ***drawbacks***; the principal is that high operating temperatures impose stringent material and processing requirements. For this reason, the present key technological challenge facing ceramic fuel cells is the development of a suitable pair of materials (electrolyte/anode and cathode/electrolyte) with a high adherence under working conditions. Furthermore, produce a pair of materials with a similar dilatation coefficient in order to reduce the residual stresses generated during the thermal fatigue produced under working conditions (cooling-heating and re-cooling process for many years). In this sense, the different constituents of the fuel cells play an important role, for this reason, more information related to each constitutive part is briefly explained in ***section 1.2.1***.

1.2.1. Parts: Cathode/Electrolyte and Anode

A ceramic fuel cell consists of two electrodes (the anode and cathode) separated by a solid electrolyte. Fuel is fed to the anode, undergoes an oxidation reaction, and releases electrons to the external circuit. Oxidant is fed to the cathode, accepts electrons from the external circuit, and undergoes a reduction reaction. The electron flow (from the anode to the cathode) produces direct-current electricity. This schematic performance is shown in ***Relations 1.1 and 1.2***.

$$H_2 \rightarrow 2H^+ + 2e^-(anode) \quad (1.1)$$

$$\frac{1}{2}O_2 + 2e^- \rightarrow O^+ (catode) \quad (1.2)$$

Ceramic fuel cells use exclusively hydrogen as fuel, and oxygen as oxidant. In theory, any gases capable of being electrochemically oxidized and reduced can be used as fuel and oxidant in a fuel cell as depicted in ***Figure 1.5***. However, hydrogen is currently the most common fuel, since it has high electrochemical reactivity and can be derived from common fuels such as hydrocarbons, alcohols, or even coal. Oxygen is the most common oxidant, since it is readily and economically available from air. For the hydrogen/oxygen reaction, to date, only oxides are being considered for use as ceramic fuel cell electrolytes as reported in Ref. [22].

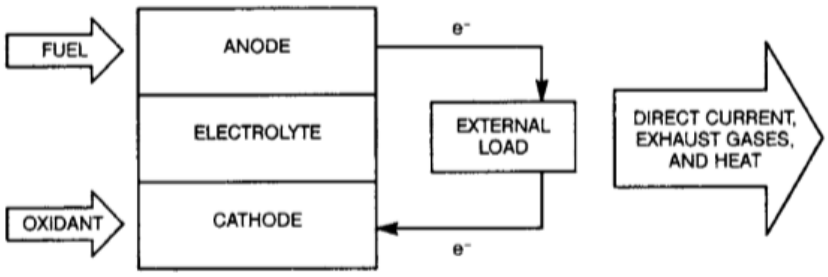

Figure 1.5: *Schematic diagram of fuel cell operation [22].*

A SOFC single cell consists of an oxide electrolyte sandwiched between an anode and a cathode. Practical SOFCs are not operated as single units; rather, they are connected in electrical series to build voltage. A series of cells is referred to as a stack, as it is presented in ***Figure 1.6***, where different SOFCs stack designs are represented.

A component, variously called an interconnect or a bipolar separator, connects the anode of one cell to the cathode of the next stack. SOFC stacks can be configured in series, parallel, both series and parallel, or as single units, depending on the particular application.

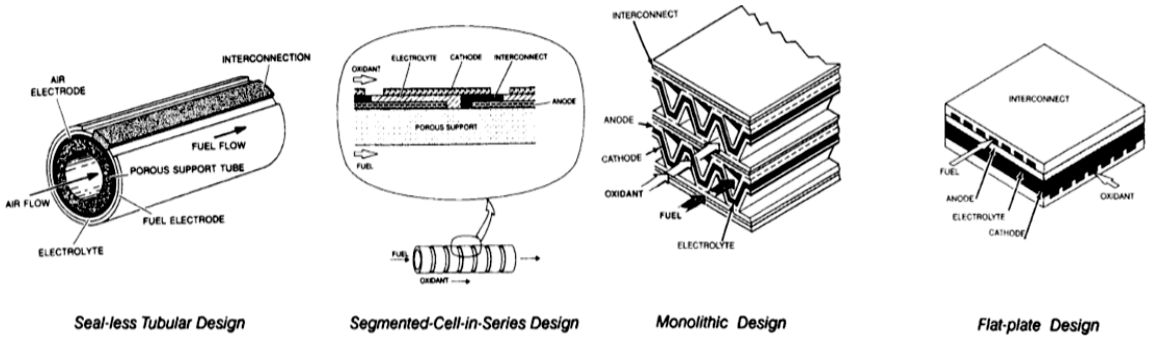

Figure 1.6: *SOFCs stack design [22].*

Each component serves several functions so they require different requirements to give stability to the SOFC, during the different reactions. In ***table 1.1***, the main requirements like: conductivity, stability, compatibility with the other components, porosity and thermal expansion, are summarized.

Table 1.1: *Requirements for ceramic fuel cell component [22].*

Components	Requirements				
	Conductivity	**Stability**	**Compatibility**	**Porosity**	**Thermal expansion**
Electrolyte	High ionic conductivity. Negligible electronic conductivity	Chemical, phase, morphological, dimensional, stability in oxidant environments	No damaging chemical interactions or interdiffusion with adjoining cell components.	Fully dense	Thermal expansion match with adjoining components.
Cathode	High electronic conductivity	Chemical, phase, morphological, dimensional stability in oxidant environments.	No damaging chemical interactions or interdiffusion with adjoining cell components.	Porous	Thermal expansion match with adjoining components.
Anode	High electronic conductivity	Chemical, phase, morphological, dimensional stability in fuel environments	No damaging chemical interactions or interdiffusion with adjoining cell components.	Porous	Thermal expansion match with adjoining components.
Interconnect	High ionic conductivity. Negligible electronic conductivity	Chemical, phase, morphological, dimensional stability in oxidant and fuel environments	No damaging chemical interactions or interdiffusion with adjoining cell components.	Fully dense	Thermal expansion match with adjoining components.

1.2.2. Types

A fuel cell electrolyte must ironically conduct one of the elements present in the fuel or oxidant. Thus, a solid electrolyte for SOFCs based on the electrochemical reactions of hydrogen and oxygen

must conduct either oxygen ions or hydrogen ions, protons. The present generation of ceramic fuel cells can be classified into two types [22]:

1. **Oxygen-ion-conducting electrolytes*: Figure 1.7*** shows the reaction of this type of electrolyte. It can be considered as an oxygen concentration cell. In this case the water is produced in the fuel side.

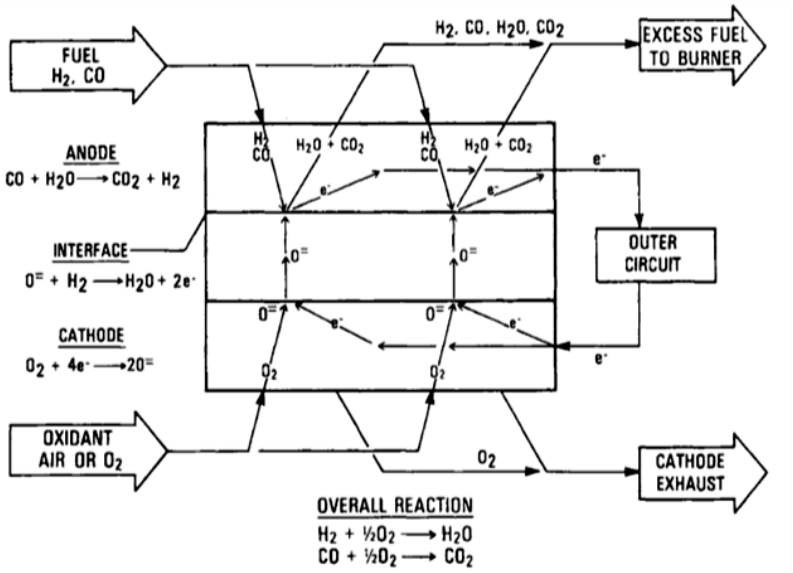

Figure 1.7: *Diagram of reactions in SOFCs based on oxygen-ion-conduction [22].*

2. **Proton-conducting electrolytes:** ***Figure 1.8*** presents the reaction of this type of electrolyte. It can be considered as a hydrogen concentration cell. On this type, the water is produced in oxidant side.

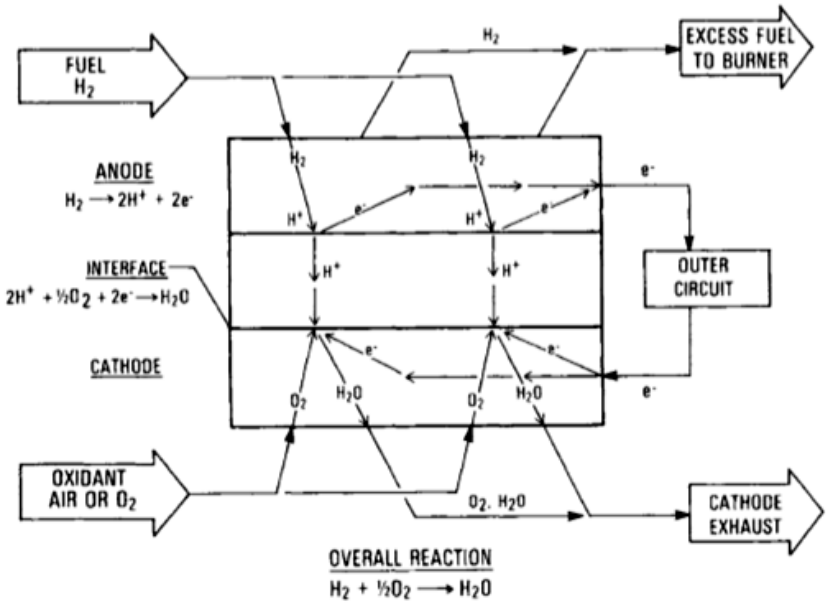

Figure 1.8: *Diagram of reactions in SOFCs based on proton-conduction [22].*

1.2.3. Characteristics

In general all kind of fuel cells present the followings characteristics [22]:

1. High conversion efficiency: The primary feature of a fuel cell is its high fuel-to-electricity conversion efficiency ranged between 45 to 60%. A fuel cell converts the chemical energy of fuel directly into electrical energy. Thus, the usual losses involved in the conversion of fuel to heat, to mechanical energy, and then to electrical energy are avoided. The efficiency of a fuel cell is further improved when the by-product heat is fully utilized (in cogeneration or bottoming cycles).
2. Environmental compatibility: Fuel cells are capable of using practical fuels as an energy source with insignificant environmental impact. Emissions of key pollutants from fuel cells are several orders of magnitude lower than those produced by conventional power generators. Production of undesirable materials such as NO_x, SO_x, and particulates is either negligible or undetectable for fuel cell systems.
3. Modularity: Fuel cells have the characteristic of modularity, i.e., cells can be made in modular sizes. Thus, fuel cell size can be easily increased or decreased. Since the efficiency of a fuel cell is relatively independent of size, fuel cells can be designed to follow loads with fast response times without significant efficiency loss at part-load operation.
4. Sitting flexibility: Because fuel cells can be made in a variety of sizes, they can be placed at different locations with minimum sitting restrictions. Fuel cell operation is quiet because a fuel cell has no moving parts; the only noises are those from auxiliary equipment. Consequently, fuel cells can be easily located near points of use such as urban residential areas as it is depicted in ***Figure 1.9***.
5. Multifuel capability: Certain types of fuel cells have multifuel capability. High-temperature fuel cells can process (reform) hydrocarbon fuels internally and do not need expensive subsystems to process conventional fuels into simple forms.

Figure 1.9: *Fuel cell system in a neighbourhood of California [23].*

1.3. SOFCs materials

1.3.1. Electrolyte

The materials that will be used as electrolyte, needs the requirements summarized in ***Table 1.1***. The most common materials employed as electrolyte are briefly explained below [22]:

1) ***Stabilized zircona:*** Stabilized ZrO_2 has been used almost exclusively as the electrolyte in SOFCs because the material possesses an adequate level of oxygen-ion conductivity and exhibits desirable stability in both oxidizing and reducing atmospheres. Among the various stabilized zircona, the Y_20_3-stabilized material (YSZ), with 3, 8 or 10% molar as the most common compositions.
2) ***Pure CeO_2:*** This electrolyte material presents a cubic fluorite structure (see ***Figure 1.10.a***) up to its melting point. Therefore, CeO_2, unlike ZrO_2, does not need any stabilization doping agent. Depending on temperature and oxygen partial pressure, the material exhibits a large oxygen deficiency with the formula $CeO_{2-\delta}$, where δ may be as large as 0.3. For small oxygen deficiencies ($\delta < 10^{-3}$), doubly ionized oxygen vacancies are the principal ionic defects with compensating electrons. For large oxygen deficiencies, a transition toward singly ionized vacancies has been observed. Pure CeO_2 has negligible ionic conductivity.
3) ***Stabilized bismuthsesquioxide:*** Pure Bi_20_3 presents a polymorphism with two different crystallographic phases: δ phase with a fluorite cubic structure (see ***Figure 1.10.a***) above 730ºC and α phase with a monoclinic structure (see ***Figure 1.10.b***) below 730 ºC. The δ phase of Bi_20_3 can be stabilized at low temperatures by doping with a certain metal oxide (like CaO or SrO). This greater ionic conductivity of stabilized Bi_20_3 offers the possibility of its use as electrolyte in SOFCs operated at reduced temperatures. The main drawback of this material is its small oxygen partial pressure range of ionic conduction. It is easily reduced under low oxygen partial pressures and decomposes into bismuth metal at an oxygen partial pressure of about 10^{-13} atm. at 600 ºC. Therefore, practical use of stabilized Bi_20_3 as SOFC electrolyte requires protection of the material from direct exposure to reducing atmospheres.

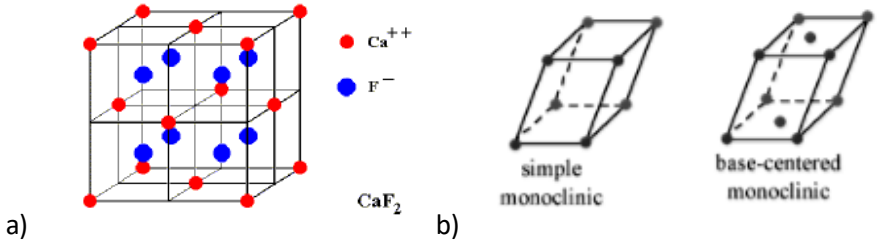

Figure 1.10: (a): *Cubic fluorite structure [25] and* ***(b):*** *Monoclinic structure [24].*

Furthermore, ***protonic conductors*** are a special class of electrolyte that comes up with some perovskite-type materials. These conductors have been known to exhibit protonic conduction in hydrogen and/or wet atmospheres at high temperatures (higher than 1000 ºC). During processing at high temperatures, oxygen-ion vacancies react with oxygen to produce electron holes. The protons that can be produced are interstitial or vacancies depends the place that they produce. From this group 2 subgroups are shown:

- ***Doped $BaCeO_3$:*** This material possess significant proton conduction at high temperatures. Though this structure does not contain any proton and the chemical formula does not include hydrogen. On the other hand, protonic conduction in the material is possible. This is because the compound incorporates water vapour from the atmosphere during preparation and subsequent cooling, and so acquires a concentration of mobile protons.
- ***Doped $SrCeO_3$:*** Doped $SrCeO_3$ is another common material being considered as a protonic conductor for SOFC applications. In hydrogen atmospheres, doped $SrCeO_3$ exhibits significant protonic conductivity. The protonic conductivity of $SrCeO_3$ based oxides has been found to increase with increasing content of oxygen-ion vacancy, but it is almost independent of the dopant concentration.

1.3.2. Anode

The materials that will be used in anode need the requirements summarized in ***Table 1.1***. The following materials widely employed as anodes are briefly explained below [22]:

- ***Nickel/Yttria-stabilized zircona cermet:*** This cermet is used almost exclusively as the SOFC anode material. This metal is preferred primarily because of its low cost (when compared with other metals such as cobalt, platinum, and palladium). To maintain the required porous structure of nickel over long periods at high temperatures and to provide other desired properties for the anode, YSZ is often incorporated as a support. The functions of the YSZ in the anode are to support the nickel-metal particles, inhibit coarsening of the metallic particles at the fuel cell operating temperature, and provide an anode thermal expansion coefficient acceptably close to those of the other cell components.
- ***Cobalt/calcium-doped ZrO_2:*** These materials are widely employed as anodes in SOFCs. Compared with nickel, cobalt has the advantage of high sulphur tolerance; however, cobalt is not commonly used because of its high cost. Also, the oxidation potential of cobalt is higher than that of nickel metal, thus requiring less complete fuel combustion.
- ***Ruthenium/YSZ cermets:*** These cermets have been tested as SOFC anodes. Ruthenium has a higher melting point (2310 ºC) than nickel (1453 ºC) thus providing better resistance to particle coarsening. These cermets have been shown to have minimum sintering at fuel cell

operating temperatures, high catalytic activity for steam reforming, and negligible carbon deposition under reforming conditions.

- ***Mixed conducting oxides:*** These oxides have also been investigated as SOFC anode materials. In mixed conductors in which both oxygen ions and electrons are mobile, the electrochemical reactions occur over the entire interfacial area. ZrO_2-Y_20_3-TiO_2 solid solutions are of particular interest for SOFC applications because of their compatibility with the YSZ electrolyte. Up to 15 mol % TiO_2 can be dissolved in ZrO_2 (stabilized with 12 mol % Y_20_3) to form a mixed conducting fluorite structure phase. The optimum composition for a mixed conducting ZrO_2-Y_2 0_3-TiO_2 anode is that at which the transference numbers or percentages of electronic and oxygen-ion conductivity are equal.
- ***CeO_2-based materials*:** These materials have been evaluated for SOFC anode applications. Doped CeO_2, exhibiting mixed conduction in the fuel reducing environment, has been studied both as anode material and as support, replacing the ZrO_2 in nickel/YSZ cermet.

1.3.3. Cathode

The main sets of materials employed as a cathode are briefly described in this section [22]:

- ***Lanthanum manganite ($LaMnO_3$):*** It has been extensively used as cathode material because of it mainly presents high electrical conductivity in oxidizing atmospheres, adequate compatibility with YSZ electrolyte, and acceptable thermal expansion match with other cell components.

$LaMnO_3$ belongs to class of perovskite (see ***Figure 1.11***) oxides of the general formula ABO_3, which presents an orthorhombic structure at room temperature and exhibits a phase transformation, from orthorhombic to rhombohedral, see ***Figure 1.12***, at about 600 ºC. This transformation has been attributed to the oxidation of some Mn^{3+} to Mn^{4+} ions. $LaMnO_3$ can present excess of oxygen, stoichiometry, or deficiency depending on the preparation conditions such as firing atmosphere, temperature, and time. And the defect of oxygen in the structure of this perovskite helps to the production of the reaction.

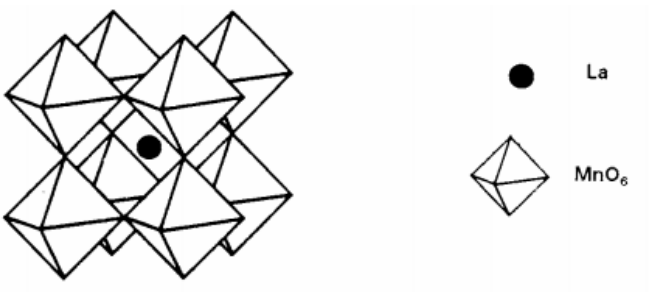

Figure 11: *Ideal perovskite of $LaMnO_3$ [22].*

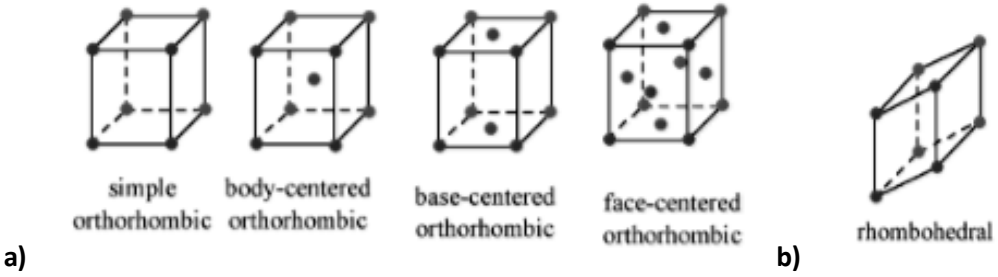

Figure 1.12: *(a) Structures of orthorhombic crystallography. (b) Rhombohedral crystallography[24].*

- ***Lanthanum cobaltite ($LaCoO_3$)***: It is another kind of perovskite of interest as SOFC cathode material. The material belongs to the same class of oxide compounds as $LaMnO_3$. This cobaltite presents a rhombohedral structure from room to 1000 ºC. Furthermore, this material presents a phase transformation from rhombohedral to cubic phase (see ***Figure 1.13***). The transformation temperature mainly depends on dopant content. $LaCoO_3$ has no oxygen excess but shows a large oxygen deficiency at high temperatures (up to 1000 ºC), especially when doped with a lower-valence cation such as strontium.

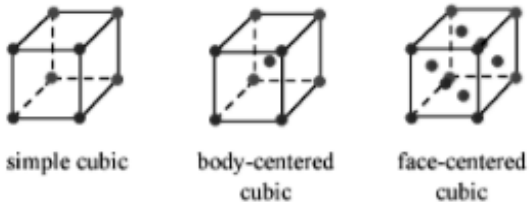

Figure 1.13: *Structure of cubic crystallography [24].*

A number of doped oxides, presented below, have been proposed and investigated as SOFC cathode materials. The disadvantages of most of these materials are related to the thermal expansion mismatch, incompatibility with YSZ, and lack of conductivity.

- ***Indium oxide (In_2O_3):*** Early SOFCs used it doped as the cathode material. This material exhibits excellent electrical conductivity under fuel cell operating conditions and can be applied as thin film by the chemical vapour deposition (CVD) method. The material performed satisfactorily for up to 5000 h without degradation. However, In_2O_3 represents the most costly and least thermodynamically stable component in the SOFC.
- ***Compounds based on $LaFeO_3$-$LaCoO_3$:*** Currently, solid solutions based on $LaFeO_3$-$LaCoO_3$ have been studied as cathode materials in reduced-temperature SOFCs due to their desirable mixed conducting properties.
- ***Strontium-doped $PrMnO_3$:*** Compositions show promise as a suitable cathode material for reduced-temperature applications.

- ***RuO_2/YSZ materials:*** These set of composite materials have also been evaluated for SOFC cathode applications.

1.4. State of art

On this Bachelor's project, three different fields may be covered: *The first one and more general is the generation of the SOFC by means of AM methodology and in particular using the robocasting technique, which is the second field covered in this Bachelor's project and finally the material used to generate the different SOFCs components (Y-ZrO_2, Lanthanum gallate strontium and magnesium doped (LSM), Nickel oxide used as electrolyte, cathode and anode respectively).*

The mix of these three fields is completely new. But there are many studies and works around SOFCs. These used to talk about which type of material are the best, which techniques used to use to get it, the geometries of the electrolyte. And all of these finish with a mechanical, electrical and thermal study, to see the improvements of the modifications.

Here, some examples of articles covering the three different field briefly mentioned above are presented and briefly summarized. All of these projects will lead to better understand the main goal of this Bachelor's project.

J. C. Ruiz-Morales, D. Marrero-López, J. Peña-Martínez, J. Canales-Vázquez, J. J. Roa, M. Segarra, S. N. Savvin, P. Nuñez, *Performance of a novel type of electrolyte-supported solid oxide fuel cell with honeycomb structure,* Journal of power sources 195 (2010) 516-521.

On this paper they use an alternative and novelty way to get the electrolyte of the SOFC. They present a honeycomb-electrolyte structure with hexagonal cells giving high mechanical properties than other structures. They use 8Y-TZP as a ceramic material for the electrolyte.

On this Bachelor's project one of the geometries that will be tried to get is the honeycomb structure. But on the paper they get this geometry by two ways; In the first one the freshly coated NOMEX mesh was left to dry (at room temperature) on a Mylar substrate film. After drying at room temperature, the sample was removed from the Mylar substrate and further dried at 200 ºC for 1 h. Several cycles of this procedure led to the closure of one side of the hexagonal cells. The second route, which yielded the same result, consisted of attaching a thin layer of YSZ prepared by tape-casting to one side of the YSZ-coated NOMEX mesh and co-firing the assembly to produce the supported structure. Slow ramp rates were used in this case to avoid cracks in the thin YSZ layer. Finally, the structure was sintered at 1400 ºC for 2 h. And on this project AM will be the leading technique to get the electrolyte of SOFCs.

J. J. Roa, J. C. Ruiz-Morales, J. Canales-Vàzquez, M. Morales, X. G. Capdevila, P. Núñez, M. Segarra, *Mechanical Characterisation at Nanometric Scale of New Design of SOFCs,* Fuel Cells 11 (2011), No. 1 124-130.

On this paper the mechanical properties, Hardness and Young modulus, of SOFCs based on YSZ and NiO-YSZ composites, have been studied. They obtained that the elastic-to-plastic transition occurred at 25 nm of penetration depth using Berkovich indenter. Also they obtained the followings values of Young modulus; for YSZ 260 ± 15 GPa and for NiO-YSZ 205 ± 20 GPa. This micromechanical property was reported for the first time in this manuscript.

All these values will be so useful to compare with the values that will be obtained at the micrometric length scale during this Bachelor's for the different electrolytes manufactured by AM technique used for SOFCs applications will.

M. Morales, J. J. Roa, J. M. Perez-Falcón, A. Moure, J. Tartaj, F. Espiell, M. Segarra, *Correlation between electrical and mechanical properties in $La_{1-x}Sr_xGa_{1-y}Mg_yO_{3-\delta}$ ceramics used as electrolytes for solid oxide fuel cells,* Journal of Power Sources 246 (2014) 918-925.

On this paper a correlation between mechanical and electrical properties of electrolytes for SOFCs has been done. The electrolyte in this case is done by Sr and Mg doped $LaGaO_3$ ceramics. And they get the samples of the electrolytes to analyse by isostatic pressing and after that a sintering process with a temperature between 1300 and 1450 ºC.

This paper will be so useful because they found a clear relation between hardness and ion conductivity. Both properties, mechanical and electrical, are strongly controlled by the electrolyte microstructure like the relative density. So it would be so interesting if this kind of relation remains stable with 8Y-TZP.

M. Morales, J. J. Roa, J. Tartaj, M. Segarra, *A review of doped lanthanum gallates as electrolytes for intermediate temperature solid oxides fuel cells: From materials processing to electrical and thermo-mechanical properties.* Journal of the European Ceramic Society 36 (2016) 1-16.

On this paper a review of SrO- and MgO-doped lanthanum gallates (LSGMs), focused on the implementation as electrolyte for SOFCs at intermediate temperature, is done. The manufacturing design, the sintering routes to lower the sintering temperatures, a chemical compatibility between electrolyte and electrodes and a study of mechanical and thermal properties, are the topics that have been covered along this review paper.

They found that with the following routes they can fabricate different cell designs without the formation of secondary phases during sintering process. Here are a brief resume of the following

routes; via preparation of well-sintered powders (citrate method, glycine nitrate method, among others) as well as the use of innovative consolidation techniques (spark plasma sintering, microwave sintering, etc), and employing sintering additives (Co, Fe, Mn,. . .). These routes allow to fabricate different cell designs without the formation of secondary phases during sintering process.

Is known that the use of interlayers between electrolyte and electrode/s increases both the complexity of cell manufacturing and the electrolyte thickness, so they get the highest performances of cells have been achieved with La-doped ceria (LDC) interlayers. The LDC interlayers act as effective barrier layers to the inter-diffusion of La and Ni between the electrolyte and anode.

G. Cai, Y. Gu, L. Ge, Y. Zhang, H. Chen, L. Guo, *Modification of electrolyte surface with "windows" and "dimples array" structure for SOFCs based on YSZ electrolyte*, Ceramics International 43 (2017) 8944-8950.

On this paper they generate a new geometry for the electrolyte surface, square mashes, using tape-casting and laser micro-processing to get it. They use 8Y-TZP as a ceramic material for the electrolyte, as in this Bachelor's project.

They found that with more "windows", they get better mechanical and electrical properties. So It will be so useful, when during this project the honeycomb geometry will be generated. Even If the hexagonal cells cannot be obtained this square mashes will be an alternate geometry to use. And It will be possible to compare the electrical properties of two different geometries in SOFC with the same technique of obtention and with the same materials.

S. Masciandaro, M. Torrell, P. Leone, A. Tarancón, *Three-dimensional printed yttria-stabilized zirconia self-supported electrolytes for solid oxide fuel cell applications,* Journal of the European Ceramic Society (2017).

On this manuscript a specific AM technique was been applied, a stereolithography 3D-dimensional printer, to get the electrolyte. They printed cells with honeycomb geometries, using 3Y-TZP as a ceramic material for the electrolyte.

During the process of fabrication several differences between the techniques applied on this paper a laser AM, and Robocasting the AM technique of this Bachelor's project, are shown.

Finally, I would like to remark that the field of Robocasting using Y-TZP is quite new, where scarce information is available in the literature. For this reason, this Bachelor's project starts a new point of view of Robocasting, with all the applications of Y-TZP and in particular a new research line in the CIEFMA's research group.

2. Goal

On this Bachelor's project, the long term goal is to be able to develop a systematic protocol to print solid oxide fuel cells (SOFC) with complex shapes by using zircona stabilized ceramic material with 8 % mol. yttrium as electrolyte with at least the same microstructural and mechanical properties as for the electrolytes manufactured by the conventional processing routes. Furthermore, in order to enhance their mechanical stability, the raw paste material will be doped with secondary phases in order to improve their mechanical properties without the need to reduce their electrical properties.

So to get on this aim, the project is divide in three different parts:

(i) To print SOFCs electrolytes with tubular and hexagonal geometries.

(ii) To evaluate and correlate the microstructural and micromechanical properties for the printed specimens in order to decide the best composition and heat treatment.

(iii) To print the electrolyte and dip the cathode in order to study and evaluate their microstructure, mechanical and electrical properties. Due to the complexity of the hexagonal geometry, this part will be conducted only in the tubular cells.

In general terms, the main scope of the project is to pretend to find the best microstructure/properties relation on a 3D printed fuel cell based on zircona material with different geometries.

Within this context, this Bachelor's project opens a new field to work with the 3D printer and in particular open a new research line in the energy field at the CIEFMAs research group, because this sector is known that is a strategic factor in the current society.

3. Experimental procedure

3.1. Materials

On this part the two principal materials employed to produce the ceramic pastes will be explained. Polymeric matrix which act as a gelling agent (Pluronic F-127® from *Sigma Aldrich (**Annexe A.1**))*, and the ceramic particles zirconia stabilized with ythria; 3, 8 and 10Y-TZP from *TOSOH (**Annexe A.2**).* The main information for each material is briefly described below in detail:

a) <u>Polymeric matrix: Pluronic F-127®</u>

The Pluronic F-127® from *Sigma Aldrich*, the datasheet is available in ***Annexe A.1***, is a copolymer used to do hydrogels, basically for medical applications.

Pluronics F-127® [28] are amphylic copolymers comprised of two external blocks of polyethylene oxide (PEO) and a central block of polypropylene oxide (PPO), comprising a global formula (PEO-PPO-PEO) as it is shown in ***Figure 3.1***. These copolymers present a thermal inverse mechanical behaviour in aqueous dissolution due to the gelling process that they suffer with the temperature; in particular when the temperature increases. This behaviour is manly originated by the difference in the critical dissolution temperature. The gelling temperature and mechanical strength of the gel depends on the concentration of polymer and the chain length of PEO and PPO.

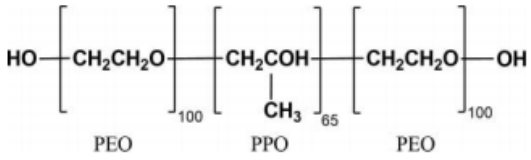

Figure 3.1: *Structural formula of Pluronic F127® block copolymer, where PEO and PPO means Polyethylene oxide and Polypropylene oxide, respectively [26].*

The behaviour of these solutions is complex, since they exhibit a liquid behaviour below the sol-gel transition temperature, which varies with the percentage of Pluronic F-127® powder as it is shown in ***Figure 3.2***, while at temperatures equal to or above this transition, their shear/viscosity module ratio undergoes an increase of several orders of magnitude in a very narrow temperature range. This nature favours its use for the Robocasting process [27]. On the other hand, in order to increase the efficiency of this gelling material, a good dispersion and homogenisation of the samples in the liquid state is required in order to obtain a stable paste suitable for the printed process.

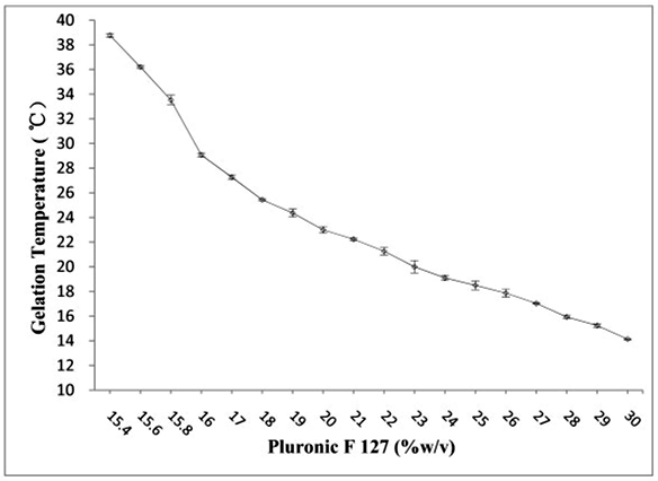

Figure 3.2: *Gelation temperature and thermoreversible behavior of Pluronic F-127® gel [28].*

b) Ceramic charge to be used as electrolyte

ZrO_2, commonly known as zircona, is a material with a long history of application in various industrial sectors. The wide variety of uses of this material ranges from its application as an abrasive when its purity is limited, to its use in blades and structural elements in highly aggressive processes due to its toughness and resistance to wear. Recently, this ceramic material has been widely employed as a biomaterial due to its chemical nature, inertness, etc.

At the microstructural level, ZrO_2 presents an allotropic phase transformation, with three different phases as it is depicted in ***Figure 3.3***. The monoclinic (*m*) phase stable at room temperature till 1170 ºC, between 1170 ºC and 2370 ºC the stable phase is the tetragonal (*t*), and above 2370 ºC the stable phase is cubic (*c*). Furthermore, the ZrO_2 material presents a phase transformation from *t* to *m* phase during the sintering processes with their consequent expansion and contraction of their unit cell, ~ 4%, generates some residual stresses that induces some cracks as a consequence producing a reduction of their final mechanical properties. However, this situation can be reversed by the use of stabilizing oxides such as magnesia (MgO), calcium (CaO), ceria (CeO_2) or yttrium (Y_2O_3), which allow the formation of multiphase materials at ambient temperature known as partially stabilized zircona (PSZ). The formation of PSZ through the ZrO_2-Y_2O_3 formulation results in the formation of a stable *t*-phase microstructure at room temperature with very high hardness and mechanical resistance, known as TZP (Tetragonal zirconia partial stabilized).

In this Bachelor's project, the zircona stabilized yttrium material will be employed with three different percentages of ytria. The Y-TZP with 8 and 10 mol. % supplied by Tosoh (***Annex A.2***) while the 3Y-TZP was supplied by Daiichi. More information about the datasheet for each ceramic material can be observed in the datasheet supplied in the ***Annex A.2***.

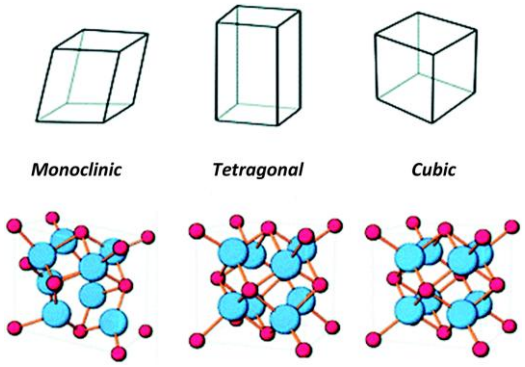

Figure 3.3: *Schematic representation of the three different phases that can present the zircona material [29].*

c) <u>Ceramic charge to be used as cathode:</u>

On the other hand, Lanthanum gallate doped strontium and magnesium (LSM), is considered as an exotic material due to it is form of rare earth metals basis will be used to make the cathode of the SOFC mixed with 8Y-TZP.

This material could have different stoichiometric relation; in general the chemical composition is presented on the following way: $La_{1-x}Sr_xGa_{1-y}Mg_yO_{3-\delta}$. And with the variation of *x, y and δ,* different types of LSM are produced depending on the desired application. The LSM used during this Bachelor's project has a $x = 0.2$; $y = 0.2$; $\delta = 0$, so the final composition is the following: $La_{0.8}Sr_{0.2}Ga_{0.8}Mg_{0.2}O_3$. It is a good candidate to be used as cathode for SOFC applications at low and intermediate temperatures, due to that it can achieve ionic conductivities as high as 0.166 $S{\cdot}cm^{-1}$ at 800ºC.

The LSM used is from *Sigma-Aldrich,* the data sheet is available in ***Annex A.3.***

3.2. Ceramic pastes

On this section two different things will be explained in detail: *(i)* the fabrication procedure as well as *(ii)* the composition of the ceramic paste that will be employed to manufacture both the electrolyte and the cathode. This consists on a mixture between three different elements: distilled water, the gelling agent (Pluronic F-127®, see ***section 3.1a***) and ceramic powder (see ***section 3.2b*** and **c**).

Currently, these type of pastes have been widely employed during the last years due to it presents a lot of different applications, being the most important for medical applications. This may be attributed to several reasons: *i)* ZrO_2 is an inherent ceramic and a bioceramic and biocompatible material with high mechanical properties and *ii)* Pluronic F-127® is a biocompatible hydrogel.

Even if in this Bachelor's project is not focused on the medical field, the Pluronic F-127 ® is a good option to use as a polymeric matrix due to their rheological behaviour.

To prepare the different mixtures, the compositions are based on the study conducted by Feilden *et al.* [30] and entitled ***Robocasting of structural ceramic parts with hydrogel inks***.

So to get the printing ceramic material, two steps are important to take into account:

(i) To make the hydrogel, which consists of a mixture between the polymeric material (Pluronic F-127®) and distilled water.

(ii) To mix the hydrogel (step *i* explained above) with the desired ceramic material and get the required ceramic paste ready to print.

In order to reach the desired ceramic printable paste, first of all it is required to prepare the hydrogel; Pluronic F-127® mixed with distilled water, during 5 min. at maximum speed, 3500 rpm. This mixture is performed by using a SpeedMixer, ***Figure 3.4***.

Figure 3.4*: SpeedMixer, the machine used to mix the hydrogel and ceramic pastes.*

As a starting point in this Bachelor's project, the ratio between Pluronic F-127® and distilled water was extracted from the data reported in Ref. [19]. In this sense, three different mixtures of 100 g of the desired gelling agent with a constant composition (25 wt. % of Pluronic F-127) were prepared along this Bachelor's project. Once the mixture between the polymeric agent and distilled water is ready it is necessary to store the mixture inside the fridge at a constant temperature (around 4 ºC) for 24 h in order to eliminate the bubbles generated during the mixing process. After that, the gelling agent is ready to prepare the ceramic base ZrO_2 pastes, following the next steps:

(1) Deposit the desired amount of the gelling agent inside of a plastic container and add the desired amount of zircona. The different compositions investigated in this Bachelor's project are summarized in ***Table 3.1***.

Table 3.1: *Different compositions for the difference tubular samples (the composition presented in this table are in wt. %).*

Sample	1	2	3	4	5	6	7	8	9	10	11	12	13	14	15	16
% of Y	8	8	8	8	10	10	10	10	3	3	3	3	8	8	8	8
% of Zr_2O	60	60	70	70	60	60	70	70	60	60	70	70	70	70	70	70

To know the proportion between de powder and the hydrogel, the previous test performed during my research stage in the CIEFMA's research group during the first semester of this year was taken into consideration. It was found that the printable region (see ***Figure 3.5***), could increase up to 70 wt. % of ceramic charge, beeing 25 vol. %. It is necessary to mention, that it is possible to print in the region of high viscosity at room temperature, without problems, yielding a final sintered specimen with densities higher than 97 %.

(2) Once the ceramic powder is included with the polymeric mixture it is necessary to mix with the SpeedMixer during 1 min at 3500 rpm. Afterwards, with a spatula mix the ceramic paste in order to homogenize the desired product and mix again in the SpeedMixer with the same conditions explained above. This process may be repeated until a homogeneous mixture without agglomeration is obtained.

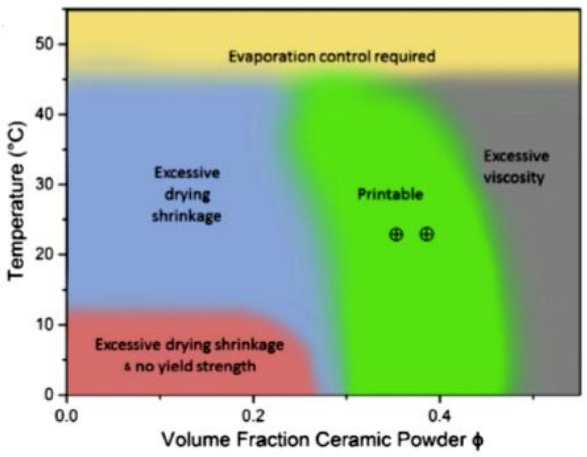

Figure 3.5*: Representation of the Temperature against the volume fraction ceramic powder, where the green region of the graph is the only printable region [30]*

In this Bachelor's project, two sets of samples were prepared with two different percentages of ceramic charge, for each type of Y-TZP employed: 60 and 70 wt. %. They were selected due to during my research stage in the CIEFMA's research group during the first semester, these conditions gave densities up to 90% with respect to the theoretical one; being this amount the starting point in this Bachelor's project.

3.3. Additive Manufacturing technique

The additive manufacturing (AM) technique that will be used during this Bachelor's project is the Robocasting technique. More information related to this methodology is extensively explained in the oncoming sections.

3.3.1. Machine: set-up

To carry out the Robocasting process, a RepRap BCN 3D+ printer supplied by the "Fundació centre CIM-Technical University of Polytechnic" with dual paste head was used. This printing machine was, adapted to print ceramic pastes as it is shown in ***Figure 3.6***.

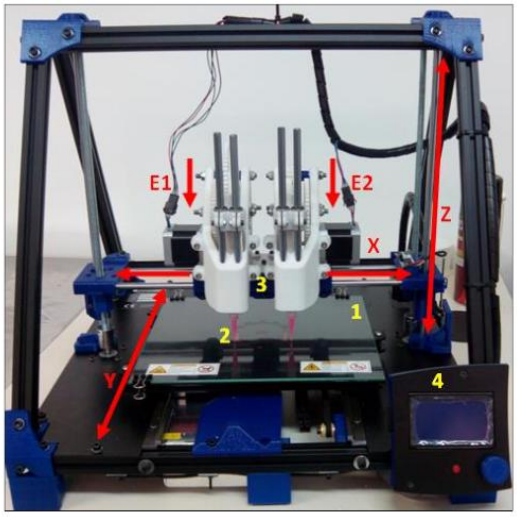

Figure 3.6: *RepRap BCN 3D+ printer used during the project.*

The three axes of the system are shown in red. The head moves on the *X*- and *Z*-axes, while the print bed moves on the *Y*-axis. The complete system consists of the following parts:

1. Printing bed: The place where the sample is printed. To minimise the adhesion of the sample to the bed, the bed is coated with cellulose filter paper.
2. Printing syringe: It acts as a printing head, and is the part of the system where the ceramic paste is loaded.

3. Print heads: These are made up of *two parts*:
    - **Base:** Attached to the printer frame. It consists of an eight-gear train that applies the force to the printing piston. The syringe fits into a hole drilled in this base.
    - **Piston:** It is coupled to the gear train by a toothed face and to the syringe by a male-female system. It is responsible for converting the rotational movement of the gears into uniaxial printing force on the ceramic paste.
4. Control knob: From where the printer functions are controlled. It contains an SD slot for loading the *gcode* files that will be selected later from the program.

3.3.2. Working conditions

The process of AM will be done at the laboratory conditions as summarized below:

- ***Temperature:*** 21ºC.
- ***Humidity:*** 70%.
- ***Pressure:*** 1 atm.

Before start to printing is so important to temperate the ceramic paste. With this the temperature of the mix increases, getting the correct viscosity. And we can avoid that the paste might precipitate before the printing process. There are different ways to do that (like heating the mixture), but the best way is to introduce the mixture in the SpeedMixer during 1 min. reaching afterwards the desired viscosity.

3.4. Printing conditions

To do the AM process there are many conditions to take into consideration and control. Apart from the conditions of the difference percentage of ceramic charge mentioned in ***section 3.2,*** and the time between the fabrication of the paste and the use of it, and the time between the printing process and the heat treatment, these are the following conditions that you may control in the AM process: *the velocity of the movements, the infill of the sample, the printing pattern, among others.* All these parameters can be controlled by the *Slic3r,* see ***Annexe B.1***, programme that transforms the files to the GCode. mode, that the machine can read.

During the printing process in this Bachelor's project, the following printing conditions were employed, see ***Table 3.2***:

Table 3.2: *Printing process conditions.*

SOFC geometry	Infill *(Figure 3.7)*	Partner *(Figure 3.8)*	Speed for print moves						Speed for non-print moves
			Perimeters	Small perimeters	Infill	Solid Infill	Bridges	Gap infill	
Tubular	100%	rectilinear	5 mm/s	5 mm/s	5 mm/s	5 mm/s	10 mm/s	5 mm/s	25 mm/s
Hexagonal	contour	Contour	5 mm/s	5 mm/s	5 mm/s	5 mm/s	10 mm/s	5 mm/s	25 mm/s

Figure 3.7 exhibits the different infills available. This printing parameter may be defined as the filling of the piece and its value goes from 0 to 100%. In the other hand the different geometries available in the printing software are summarized in ***Figure 3.8***, being the linear and the honeycomb geometry the patterns employed in this Bachelor's projects in order to print the tubular and the honeycomb electrolytes, respectively.

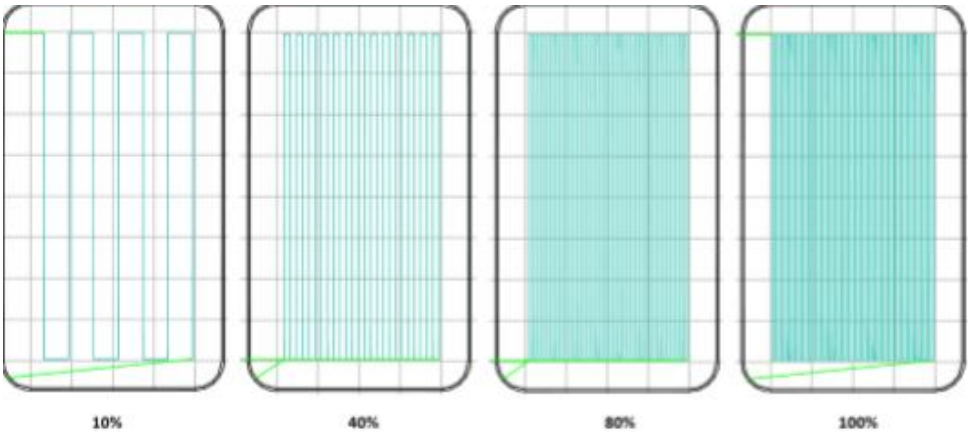

Figure 3.7: *Examples of different infills for print the samples [31].*

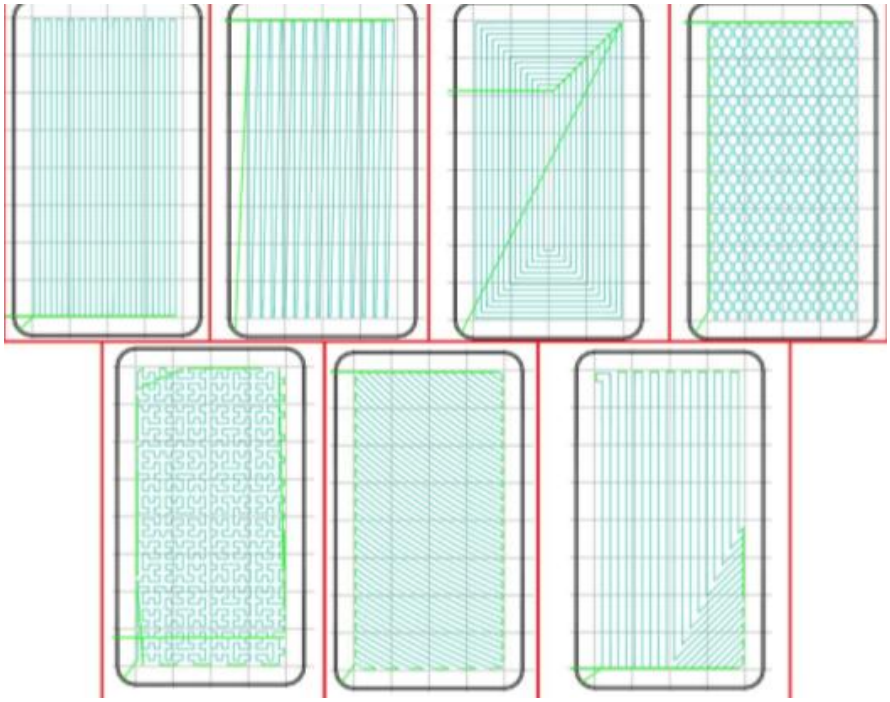

Figure 3.8: *From left to right and top to bottom: Rectilinear, line, concentric, honeycomb, hilbertcurve, archimedeanchords, octagramspiral [31].*

The other condition that in this Bachelor's project will be applied to the SOFC is the geometry. In this work two different geometries were investigated:

- Tubular (see ***Figure 3.9.a***) and Hexagonal (see ***Figure 3.9.b***).

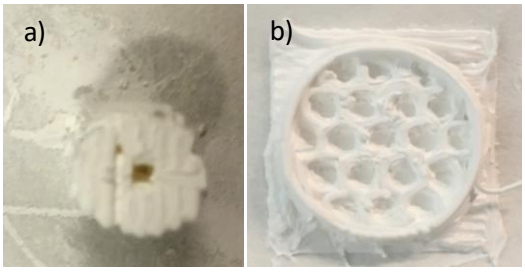

Figure 3.9: *Green body samples of the two different geometries. a) Tubular geometry, b) hexagonal geometry.*

3.5. Sintering process

This step becomes relevant during the process of obtaining the final specimen. In this type of manufacturing process, the parts cannot be compact due to the complex shapes and/or geometries. Within this context, the sintering process is a key step in order to densify the green bodies and reach

the desired microstructure and mechanical properties. The sintering process of the different specimens was made on a *Nabethern* furnace, see ***Figure 3.10.***

Figure 3.10: *Furnace where the printed specimens were sintered.*

Along this Bachelor's project has an added complication: geometries are a bit complex, because due to their shape, the printed specimens can present stress concentrators. In order to densify the specimen and get a final printed sample with the desired microstructure and mechanical properties several treatments were tried in order to:

(1) Avoid the brittle breakage of the pieces,
(2) To obtain densities greater than 90% with respect to the theoretical one, and
(3) To get printed specimens microstructurally and mechanically similar than those obtained by the conventional ceramic routes.

Three different thermal treatments (T.T.) were investigated along this Bachelors projects. The main T.T. conditions are summarized in ***Table 3.3,*** and the T.T applies are represented in ***Figure 3.11.***

Table 3.3: *Summary of the T.T conditions for each treatment.*

T.T	A	B	C
1st heat speed	2.9 ºC·min^{-1}	2.9 ºC·min^{-1}	1.5 ºC·min^{-1}
1st stop	700ºC - 1h	700ºC - 1h	700ºC - 1h
2nd heating speed	3.125 ºC·min^{-1}	3.125 ºC·min^{-1}	1.56 ºC·min^{-1}
2nd stop	1450ºC - 2h	1450ºC - 5h	1450ºC – 2h
Cooling down speed	2.9 ºC·min^{-1}	2.9 ºC·min^{-1}	1.5 ºC·min^{-1}

Prior to microstructural and mechanical properties determination, the specimens were carefully polishing following the process described in ***section 3.6***.

Figure 3.11*: Representation of the different T.T. a) T.T. a, b) T.T. b, and c) T.T. c.*

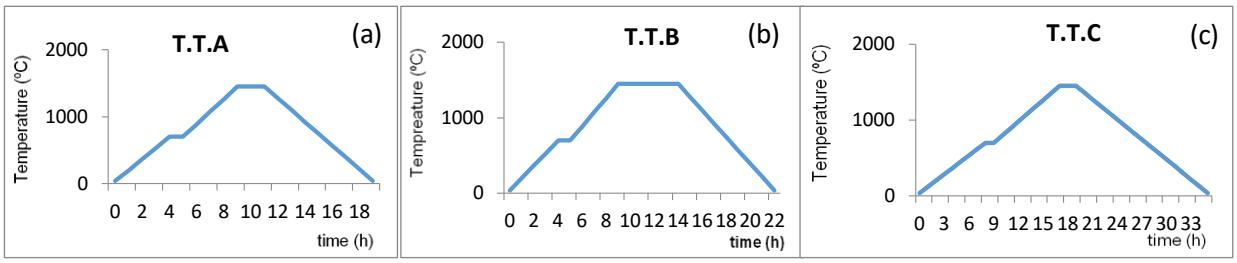

3.6. Polishing process

The polishing method is an experimental procedure, done with frequency prior to the microstructural and mechanical characterization. In this Bachelor's project, this process is required in order to get a smooth surface in order to evaluate their micromechanical properties by using the Nanoindentation technique, mainly the Hardness and elastic modulus, as well as to evaluate their microstructure and defectology produced during the printing process present in the printed samples by using advanced characterization techniques, like the field emission scanning electron microscopy, the laser confocal microscope among other advanced characterization techniques described along the experimental part section.

During this step, two different requirements are necessary to be reached: (1) Planarity of the specimen as well as (2) to get a mirror surface.

This part can be summarized in two different steps:

a) **Sample preparation:** In order to be able to easily prepare the specimen (decrease the roughness) and reach the planarity of the printed sample, they were embed in an epoxy resin, (the data sheet is available in ***Annexe A.4***), as it is shown in ***Figure 3.12***.

Figure 3.12: *Hexagonal samples put inside the resin to polish them.*

b) **Polishing process:** The polishing process was done in a conventional polishing machine from Struers (LAboPol-5), see ***Figure 3.13.a***. Also different polishing papers with different grid size of SiC, and diamond suspensions with different particle size were used; all of them shown in ***Figure 3.13.b***. ***Table 3.4*** summarize the main parameters employed in the polishing process.

Table 3.4: *Summary of the different parameters employed during the polishing process.*

Step	1	2	3	4	5	6	7
V (rpm)	200	200	200	200	200	200	200
Polishing paper	Sandpaper P:120	Sandpaper P:320	Sandpaper P:600	Sandpaper P:1200	Polishing cloth	Polishing cloth	Polishing cloth
Suspension	Water	Water	Water	Water	6µm	3µm	SiO_2 colloidal

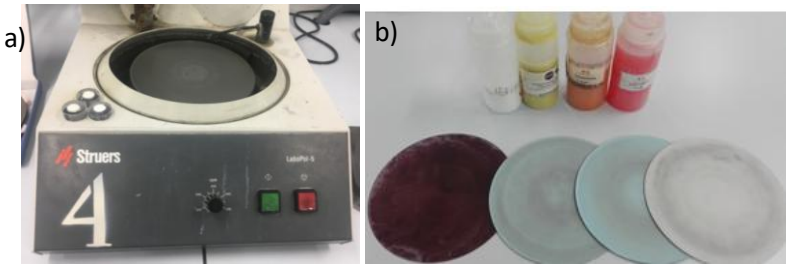

Figure 3.13: *a) Polishing machine of the brand Struers, model LaboPol-5 and b) polishing clothes and suspensions used during the polishing process.*

3.7. Dip coating

Once the electrolyte is ready, the cathode may be deposited. In this sense, the dip coating technique was employed to deposit the cathode on the pre-sintered 8Y-TZP electrolytes. This technique is commonly used in the surface industry due to it is easy to apply, fast and effective if it is well applied on a pre-treated surface.

It is important to emphasise that this technique was been applied just tubular samples. The reason is the geometry. The tubular one has more specific surface, if the dip coating does not works on them, in hexagonal one does not work too.

In order to improve the adhesion between the electrolyte and the cathode, the electrolyte was pre-sintered at 1100 ºC as it will be described below. After that, the cathode solution was prepared and subsequently the electrolyte was dip this solution and it is left inside for a certain period of time. Finally, the T.T.a, see ***section 3.5***, is applied.

As it has been briefly mentioned above, four different steps may take into consideration:

1. Pre-sintering process: This treatment increases from room to 700 ºC at a constant heating speed of around 1.5 ºC·min^{-1}. After that, the temperature was held constant to 700ºC for 1 h; during this segment, the hydrogel is burning and eliminate from the printed specimen. Subsequently, the temperature increases till 1100ºC at a constant heating rate of 1.56 ºC·min^{-1} and held constant for 2 h. Finally, the temperature decreases until room temperature at a constant cooling speed, 1.5 ºC·min^{-1}. . A schematic representation of the T.T: diagram is shown in ***Figure 3.14*****.**
2. Solution: The powders were a mix of 60 wt % of Lanthanum gallate strontium and magnesium doped (LSM) with 40 wt % of 8Y-TZP. The mixing of these powders were mix with an hydrogel composed by 25 wt % of Pluronic F-127® and 75 wt % of distilled water following the process described in **section 3.2.**
3. Sintering process: It was been applied the heat treatment A (see ***section 3.5, Figure 3.11.a***).
4. Times: ***Table 3.5*** summarized the five different conditions of times applied to the different electrolyte samples.

Table 3.5: *Summary of the five different conditions employed to coat the tubular SOFC electrolyte.*

Samples	1.A	1.B	1.C	1.D	1.E
Immerse time	15''	30''	60''	60''+60''	60''+ 60''+ 60''
Dry time between next immersion	0''	0''	0''	60''	60''
Total time	15''	30''	60''	180''	300''

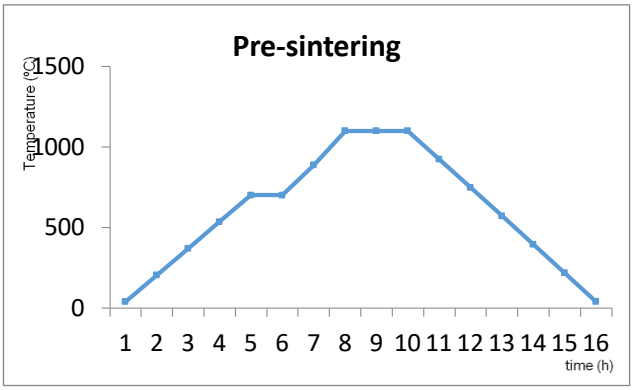

Figure 3.14: *Representation of the pre-sintering treatment.*

3.8. Characterisation techniques

The main techniques employed to microstructurally and mechanically characterise the ceramic printed specimens are briefly explained along this section.

3.8.1. Density

The study of the density of the printed part is decisive for the analysis of the results; since it indirectly gives the percentage of internal porosity as well as this parameter will lead to compare the quality of the printed specimens with the specimens manufactured by using the conventional ceramic processing routes.

The aim of the study is to obtain SOFC's electrolytes and these specimens need to have good mechanical properties to maintain the geometry and the structure. So all samples may acquire a relative density higher than 90 %. For this reason, the specimens with less than 90% will be excluded from further microstructural and mechanical analysis.

The density of the pieces has been determined by the Archimedes method by using the equipment presented in ***Figure 3.15***, which is based on the Archimedes principle. It says that by submerging a body into a fluid it receives an upward thrust proportional to the density of the fluid, the volume of the submerged body and the gravity of the earth. In this sense, measuring the relative mass of the body when submerged in distilled water and the mass of the body in air, the thrust force can be determined.

All the measures were made in a balance from *Mettler Toledo*, model xs3035, as it is depicted in ***Figure 3.15***. With the ***equation 3.1***, the density value can be determined.

$$\rho = \frac{A}{A-B} \cdot (\rho_o - \rho_L) + \rho_l \, , with \; \rho_o = 1 \frac{g}{cm^3} \;\; (auxiliary \; fluid); \; \rho_L = 0.0012 \frac{g}{cm^3} \qquad (3.1)$$

Where *A* and *B* in this equation represents the weight of the specimen in air and in the fluid employed (distilled water), respectively.

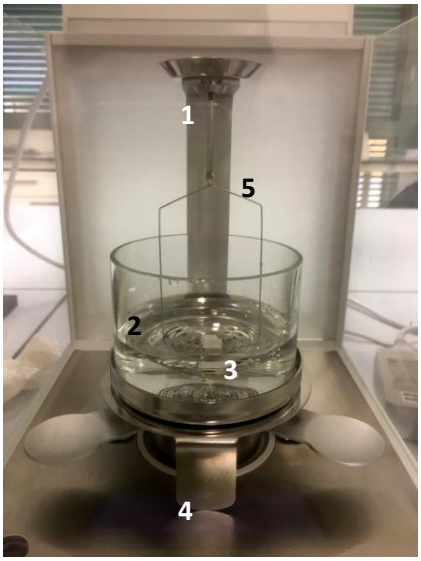

Figure 3.15: *Archimedes method set-up.*

In the ***Figure 3.15***, the difference parts of the balance are shown:

1. Platform to locate the sample to calculate the weight of the sample in the air.
2. Recipient to fill the fluid (distilled water) to submerge the sample.
3. Platform to place the sample to calculate the weight of the sample in the water.
4. Zone to support the recipient of the water.
5. Support to join the part 1 and 2.

Furthermore, it is necessary to highlight that the environmental conditions may take into consideration, being these:

- **Temperature:** 22ºC
- **Auxiliary fluid:** distilled water
- **Principal fluid:** air

Mainly, the density for all the printed samples were determined by the method explained above. However, two specimens presented an abnormal trend (values higher than 100 %), samples 13 and 14 (see ***Table 3.1***, **section 3.2**). Within this context, the helium pycnometer was used, see ***Figure 3.16***.

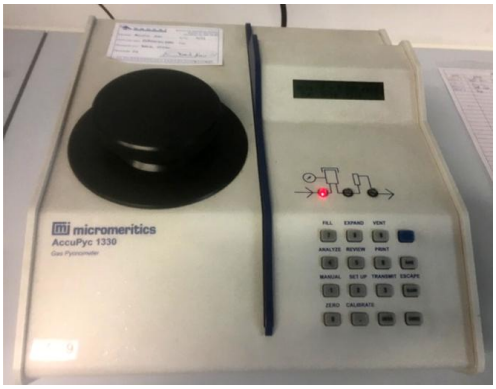

***Figure 3.16**: Helium pycnometer used during the Bachelor's project, to measure the density of samples 13 and 14.*

This technique is based on the equation of the ideal gases (*see **equation 3.2***). It says that the product of the pressure (*P*) that makes a gas inside a chamber with the volume (*V*) of this chamber is proportional to the product of the number of moles (*n*) of the ideal gas applied with the temperature (*T*) inside the chamber and with the constant of the ideal gases (*R = 8.314 J/(K·mol)*).

This technique works on the following way: the sample is introduce in the chamber of the machine (see ***Figure 3.16***) labelled (1)***,*** and a gas, in this case Helium (He), is injected. The pressure that this gas is injected is known, so using the ***equation 3.2***, the system knows the volume injected inside the chamber.

$$P \cdot V = n \cdot R \cdot T \qquad (3.2)$$

After that different types of chambers can be used, with known sizes. You programme in the machine which you will use. So with the difference between the volume of helium and the volume of the chamber, the machine gives to you the volume of your sample.

Finally, using the ***equation 3.3****,* and knowing the weight of each sample, the density can be calculated.

$$\rho = \frac{m}{V}\ (g/cm^3) \qquad (3.3)$$

After that, to do an easier way to compare results the relative density was been calculated. Using theoretical density for each ZrO_2 specimen sintered by conventional processing routes, like cold isostatic pressing, it was calculated using the ***equation 3.4***. And as a consequence of this measurement, the percentage of porosity of the printed samples could know, because it would be the difference between 100% of density and the real relative density.

$$\%\rho = \rho \,/\, \rho_T \qquad (3.4)$$

3.8.2. Dimensions

Due to the importance of the geometry, the final dimensions of the samples were been calculated to see the reduction during the heat treatments, and to get the dimensions desired. A magnifying glass was been used. It use a lens that could magnify the image with the help of a light

The magnifying glass used during this project was an Olympus SZX16, see ***Figure 3.17.*** To study the samples different lens were used:

- **x0.7:** To big geometries like the external diameter of the tubular samples.
- **x0.8:** More specific zone, like the internal diameter of the tubular samples, or the wall thickness from the hexagonal samples.

Figure 3.17: *Magnify lent used during the project.*

3.8.3. Optical Microscope

An optical microscopy (OM) is a type of microscope which uses visible light and a system of lenses to magnify images of small samples. It will be used to check the surface porosity and defects of the different printed sample.

The OM used during this project was an Olympus BX53M microscope, see ***Figure 3.18.*** To study the samples different lens were used:

- **x10**: To have a general image of the superficial porosity and of the printing defects.
- **x20:** To magnify a specific defect or porosity to study the geometry of them.
- **x50**: To see the interphase between the sample and the cathode deposited.

Figure 3.18: *OM used during the project.*

The nature of the internal porosity and defects is needed to study, because the relation between these parameters and the mechanical properties was helped to explain the influence of all the parameters during the conformation and processing of samples. The analysis was consisted in a study of the size, the distribution and the geometry of the porous. To go away with this part was used an OM.

3.8.4. Atomic Force Microscope

To make an accurate study of the topography of the sample an atomic force microscopy (AFM) was used. It measures forces between a sharp probe (with a tip diameter <10nm) and surface at very short distance, 0.2 – 10 nm probe-sample separation, providing a 3D profile of the surface of the sample even at nano-lenght scale. A flexible Si cantilever supports the probe and the AFM tip touches the sample surface and simultaneously registers the force between the probe and the surface [32].

The movement of the probe is typically measured by a “beam bounce”. A semiconductor diode laser is bounced off the back of the cantilever against a position sensitive photodiode detector. This detector measures the bending of the cantilever resulting from the tip scanning over the sample. The deflections measured by the cantilever, are used to generate a map of the surface topography [33]. A schematic figure of an AFM is represented in ***Figure 3.19.***

The AFM has normally three operation modes:

i. **Contact mode:** the tip is in contact with the surface and the separation between the probe and surface is less than 0.5 nm, it experiences repulsive Van der Wals forces.
ii. **Tapping mode:** the tip zooms in and out in a probe-surface separation of 0.5 to 2 nm. In this project this was the working operation mode.
iii. **Non-contact mode:** in this case the probe-surface separation is around 0.1 to 10 nm.

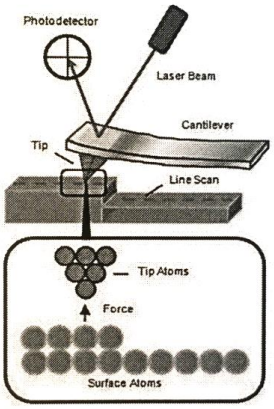

Figure 3.19: *Schematic representation of AFM equipment [32].*

For this Bachelor's project the Dimension D3100 (Veeco), see ***Figure 3.20,*** was used to study the superficial porosity and the residual indentation imprints.

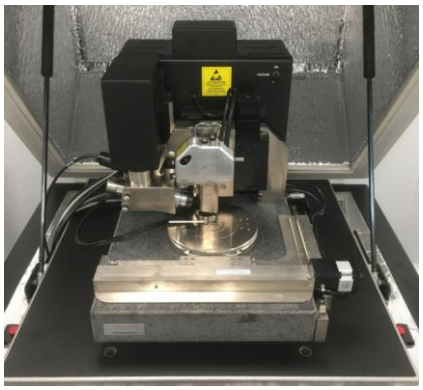

Figure 3.20: *AFM set-up used during the project.*

3.8.5. X-ray diffraction

X-Ray diffraction (XRD) technique consists in a beam of electrons accelerated, that impacts to a target material, producing the interaction between the electrons and the material.

All crystalline solids consist of a regular arrays of atoms, ions or molecules with interatomic spacing on the order of 100pm or 1 Å. There will be a part of the incident beam that will be absorbed by the material and the other one will be reflected. This reflected part is the beam that the machine detects in a wavelength. For each material and different phase that exists, there are a wavelength associated to them.

An XRD equipped with a PIXcel3D detector was used, see ***Figure 3.21,*** to record the XRD patterns of the crystallography phases present on the 8Y-TZP powder used during the project to make the ceramic pastes.

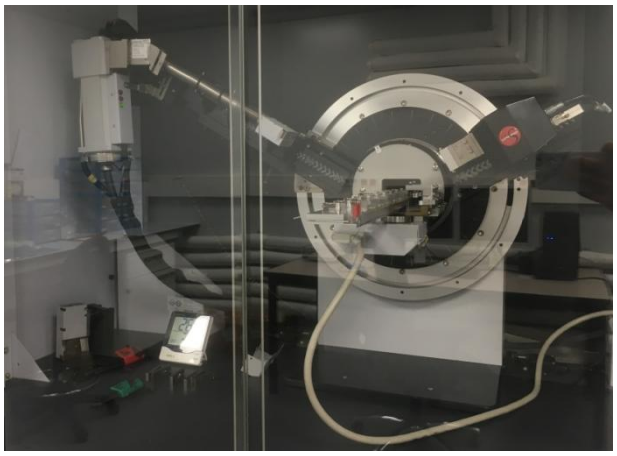

Figure 3.21: *XRD equip used during this project.*

During this project the XRD was worked under the following conditions:

- **Step size:** 0.02º.
- **2-Θ range:** 20º to 90º.

3.8.6. Field Emission Scanning Electron Microscope

Field Emission Scanning Electron Microscope (FESEM) is a Scanning Electron Microscope (SEM) based technique. SEM uses a focused beam of high-energy electrons to generate a variety of signals at the surface of solid specimens. The image is formed in the SEM by an electron beam that crossing the sample scans it and collects the signals that derive from electron-sample interactions. Theses interactions reveal important microstructural information like: texture, chemical composition, crystalline structure and orientation of materials. FESEM also employs a beam of highly energetic electrons and the concept field appears by the generation of an electric field, because the surface of the samples is conductor. For this process, the equipment requires an extreme vacuum in the column of the microscope (around 10^{-6} Pa). FESEM involves an electron emission cathode and anodes, see ***Figure 3.22.a***. The acceleration voltage between these electrodes is commonly in the range of 0.5 to 30 kV [34].

An electron detector perceived the secondary electrons emitted, and the image is created by comparing the intensity of secondary electrons to the scanning primary electron beam [35]. The ***Figure 3.22.b*** shows the model of FESEM used during the Bachelor's project:

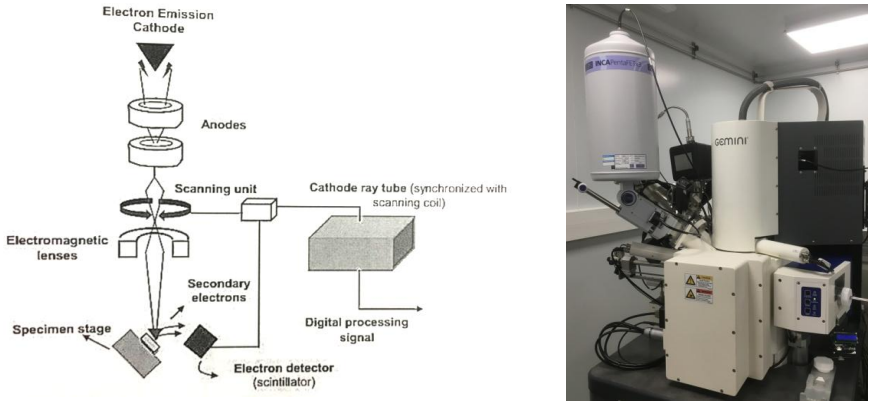

Figure 3.22: *a) FESEM schematic representation [35]. b) FESEM model used during this Bachelor's project.*

In this Bachelor's project the FESEM was used to study the superficial porosity the indentations generate in the sample and also to study the grain size.

3.8.7. Focused ion beam

Focused ion beam (FIB), in a simple definition is an instrument that resembles a SEM. SEM uses a focused beam of electrons to image the sample while FIB setup uses a focused beam of ions instead. The ***Figure 3.23*** shows a schematic image of the equipment.

The operation principle of the FIB microscope consists of sputtering atoms onto a target material, with a high energetic Gallium ion beam, Ga+. The ion are generated from a Ga liquid metal ion source composed of a Ga reservoir mounted above of a tungsten needle. Ga source is heated up to its melting point and then it flows to the tip of the needle. An intense electric field is produced at the source tip that ionizes the gallium, draws the liquid metal into the fine tip, of about 2-5nm in diameter, and extract ions from narrow tip. The Ga+, are accelerated down the column in an electrical field of about 30 KV and sputtered over the region of interest [36].

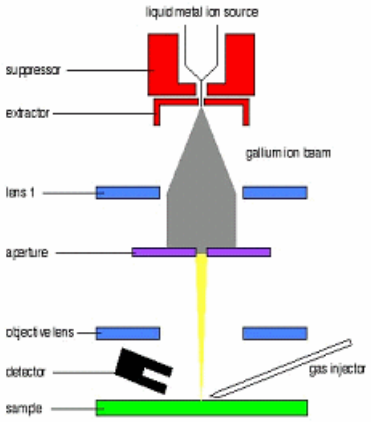

Figure 3.23: *FIB schematic representation [37].*

The aim to use this technique during this process is to get images of the damage effect produce by the cub-corner indentations in the surface of the sample. Also this technique is interesting to if the porosity of the sample is superficial or not. In this Bachelor's project the subsurface damage induce during the cube-corner indentation were inspected by means of FIB. Cross-sectioning and microscopy were conducted using a dual beam Workstation (Zeiss Neon 40) with an ion beam current of 500 pA.

3.8.8. Micromechanical properties: Nanoindentation technique

Hardness (*H*) has been defined as "material's resistance to plastic deformation". The term *H* may also refer to resistance to bending, scratching, abrasion or cutting. The usual method to achieve a *H* value is to measure the depth or area of an indentation left by an indenter of specific shape, with a specific force applied for a specific time.

The results of this test are dependent on the scale and the test method. So depending on the characteristics of the indentation and the strain field, mechanical testing methods can be classified as macro-, micro-, nano- and pico-indentations.

In this Bachelor's project, the nanoindentations were applied in order to determine the mechanical properties (hardness and elastic modulus) as well as to induce cracks and determine the fracture toughness by using two different indentation tips Berkovich and cube-corner, respectively (see ***Figure 3.24***).

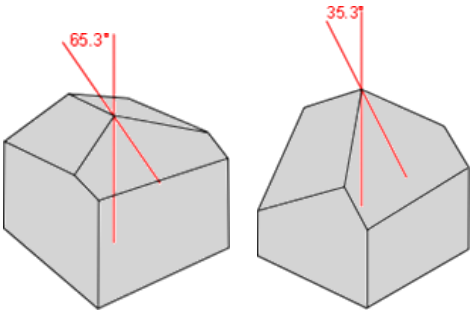

Figure 3.24: *a) Berkovich tip. b) Cube-corner tip. [38]*

Hardness and elastic modulus (Berkovich indentation):

The Berkovich tip is a three-sided pyramid. The angle between the centreline and the three faces is 65.3º. The three face design allows grinding the tip to a sharp point. It is suitable for bulk materials, thin films, polymers, scratch testing and wear testing [38].

In this Bachelor's project the Berkovich tip was used in order to measure the hardness *H*) and the elastic modulus (*E*) at the submicrometric length scale.

Hardness (*H*) and elastic modulus (*E*) are the most commonly measured properties as a function of the displacement into the surface (*h*) determined during a nano-indentation essay. The method of Oliver and Pharr is used to directly determine the micromechanical properties through the loading-unloading or *P-h* curve. This methodology allows determining on a direct way both mechanical properties. This method can obtain these information thanks of the data obtained during one cycle of loading and unloading, from an indentation of the material.

In particular, to get the values of these properties the procedure is based on the unloading process shown schematically in ***Figure 3.25***, in which it is assumed that the behaviour of the Berkovich indenter can be modelled by a conical indenter [39].

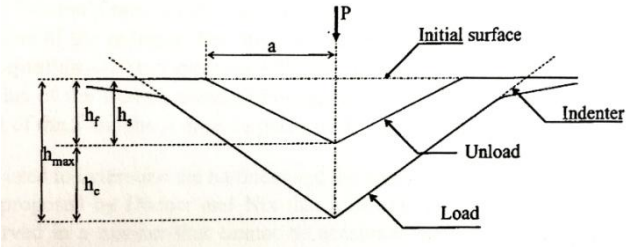

Figure 3.25: *schematic illustration of the unloading process showing parameters characterizing the contact geometry [40].*

Three are the principal conditions that you can control: the number of indentations per test, the distance between each indentation and the depth of the print. These two last one are really important. During an indentation essay, the print that generates the tip has a zone with an elastic deformation and when the applied stress is higher than the yield strength of the material the plastic deformation zone appears. The elastic deformation zone is near 20 times the maximum displacement into the surface, while the plastic zone has a rate of 7 to 10 times the maximum penetration depth. For this reason to avoid the influence of the plastic zone to other indentation and slightly modify the hardness value, the distance between imprints at least may be keep constant and equals to 7-10 times the displacement into surface.

To make this essay on this Bachelor's project and attempting to evaluate the composite hardness and elastic modulus for the printed specimens, a homogeneous array of 25 imprints (5 by 5) was performed by using the Berkovich indenter. This array was performed at 2000 nm of maximum displacement into surface or until reaching a maximum applied load of 650 mN by using a nanoindenter XP (MTS, see ***Figure 3.26***) equipped with a continuous stiffness measurement (CSM) module, the later allowing a dynamic determination of the mechanical properties during the indentation process. A constant distance around 50 μm was held between each imprint in order to avoid any overlapping effect. Along the indentation process, the indentation strain rate was held at 0.05 s^{-1}.

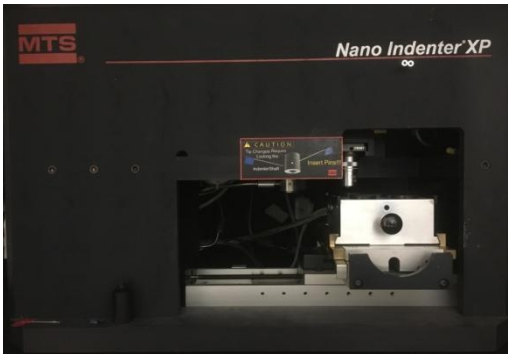

Figure 3.26: *Nanoidenter set-up used during the project.*

Fracture toughness: Cube-corner indentation

The cube-corner tip is a three-sided pyramidal tip with perpendicular faces like the corner of a cube, see ***Figure 3.24.b***. The centreline-to-face angle is 35.3º. It is suitable for thin film, scratch testing, fracture toughness and wear testing [38].

In this Bachelor's project a cube-corner tip was used in order to induce damage into the samples, mainly in order to induce damage and be able to study the fracture toughness of the printed samples.

The sharper cube-corner indenter produces much higher stress and strain in the vicinity of the contact, which is useful, for example in producing very small, well defied cracks around the residual imprint in brittle materials like ceramic materials; such cracks can be used to estimate the indentation fracture toughness at small length scales.

The indentation fracture toughness, K_{IC}, depends on different kind of parameters, like intrinsic and extrinsic parameters, etc. When cube-corner indenters are used, the proper equation (see ***equation 3.5***) may be used to determine the K_{IC}. In this Bachelor's project, the K_{IC} is determined by using the Laugier equation [41]:

$$K_{IC} = 0.057\,(\frac{l}{a})^{-\frac{1}{2}} \cdot (\frac{E}{H})^{\frac{2}{3}} \cdot \frac{P}{c^{2/3}} \qquad (3.5)$$

where E and H are the elastic modulus and the hardness of the material respectively; l is the crack length from the indentation corner, a is the indentation diagonal and $c = l + a$, this relation is shown in the ***Figure 3.27*** [41].

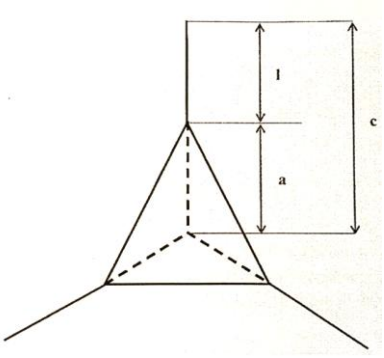

Figure 3.27: *Crack parameters [39].*

On this Bachelor's project, five different loads were applied (10, 20, 30, 40 and 50gf), making 5 indentation for each load.

Nanoscratch

The Nanoscratch tests were conducted by using a Nanoindenter XP (MTS) (see **section 3.8.7**). This technique allows us to induce complex stress field into the material as well as evaluate the tribological properties of the material.

During a nanoscratch test, four parameters may take into account: -normal force, normal displacement, lateral force and lateral displacement. All of them,-are measured and recorded as a function of time. From these parameters, comprehensive information about a material's nanoscratch properties can be characterized. Commonly characterized nanoscratch properties include friction between the sample surface and scratch diamond probe, critical load (P_c) of interfacial failure, and scratch resistance can be easily determined. Furthermore, this technique can also be used to study the scratch resistance by quantifying the minimum load for generating visible damage, like Chevron cracks, spalling, among others [42].

Figure 3.28, shows schematic representation of a nanoscratch linear test.

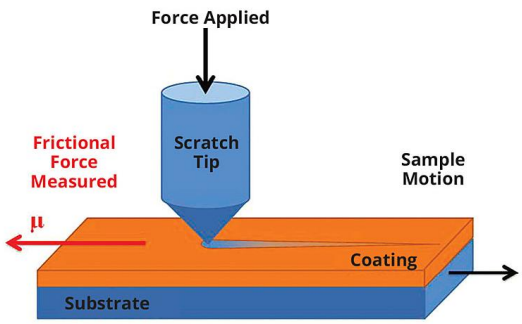

Figure 3.28: *Nanoscratch linear test [42]*

During this Bachelor's project, the nanoscratch tests have been conducted under the following conditions:

- **Applied load range**: 0 to 50 mN.
- **Length:** 250 µm.
- **Velocity:** 10 µm/s.
- **Working mode:** linear incremental load.

4. Results and discussion:

4.1. Microstructural parameters:

4.1.1. Dimensions

The results that will be present in this part are obtained using a magnify lent (see ***section 3.8.2***). With the help of lent some low images were done of the tubular and hexagonal electrolytes and subsequent by using the *ImageJ* (see **annex B.2**), software, the different measures were taken. ***Figure 4.1,*** shows many example images of the tubular (***Figures 4.1.a*** *and* ***b***) and hexagonal electrolytes (***Figures 4.1.c*** *and* ***d***).

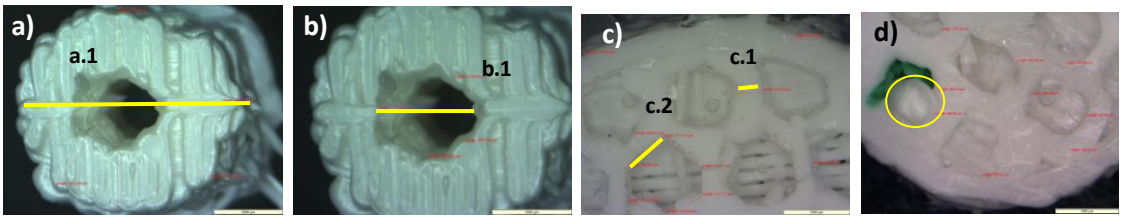

Figure 4.1: *a) Image of the tubular geometry at x0.7. b) Image of the tubular geometry at x0.8. c) Image of the hexagonal geometry at x0.8. d) Image of the sample B at x 0.8.*

The ***Figure 4.1.a*** shows the line ***a.1,*** which will lead to measure the outer diameter for the tubular geometry, while the line **b.1** presented in ***Figure 4.1.b***, the inner diameter is evaluated. Also for each sample four random measures like those presented in ***Figure 4.1.d***. On the other hand, for the honeycomb electrolyte (***Figure 4.1.c***), two different measurements were done, **line *c.1*** and ***c.2***, where the thickness of the wall and the hexagon side are measured, respectively. Finally, in ***Figure 4.1.d*** are shown the geometries used to measure the area of sample B, where the hexagon shape is not so evident. In this particular case, six measures were taken per specimen.

In the case of the tubular geometry with the cathode, the cathode thickness (see ***Figure 4.2***) was directly determine by using the OM technique (see **section 3.8.3**), six images were taken and five measurements per image were randomly taken in order to get a statistical signification. Afterwards, they were measured by the *ImageJ* software. Furthermore, as it is evident, the microstructural OM images shows a dense electrolyte, which fits perfectly with the density data presented in ***Table 4.4***, while the cathode presents a high pore density, which is intended to facilitate the electronic conduction of the SOFC.

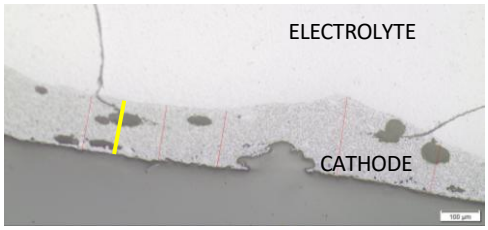

Figure 4.2: *Image of the tubular geometry (electrolyte/cathode).*

Table 4.1 and 4.2 summarizes the dimensions for the geometries. As it is evident in this table, for the tubular geometry, the theoretical value for the outer diameter is 10,000 µm, and for the inner diameter is 3000 µm. Compared the theoretical values designed with the *Solidwords (**Annexe B.3**)* with the finals values after the sintering process; see ***Table 4.1***, a reduction of around 30-40 % is produced. There are two factors that contribute on that; the losing of water the days before the sintering process and also during the sintering process.

Table 4.1: *Summary of the average for the outer and inner diameter dimensions for tubular geometry*

Sample	13	14	15	16
Outer diameter (µm)	6230 ± 133	6169 ± 175	6215 ± 93	5884 ± 282
Inner. diameter (µm)	1994 ± 150	1639 ± 55	1973 ± 164	2441 ± 232

On the other hand, for the hexagonal electrolyte geometry, the theoretical designed dimensions performed before to print the complex electrolyte were: wall thickness is 840 µm and for the hexagons side is 1.63 mm. Comparing the designing dimensions with the experimental values obtained after the sintering process, see ***Table 4.2****,* a reduction of around 30% in the side hexagon is produced. However, in the case of the wall thickness a reduction between 10 to 20 % is produced. For this particular and complex structure, the contraction induced due to the sintering process is not homogenous. Within this observation, we may consider that the hexagonal electrolyte will presents some residual stresses due to two different factors: *(i)* different contraction inside the specimen will create some residual stresses, and *(ii)* the sharp edges that this geometry presents.

Table 4.2: *Summary of the average dimensions for the hexagonal electrolyte geometry.*

Samples	Hexagon side (µm)	Complex geometry (mm^2)	Wall thickness (µm)
A	1178 ± 217	-	775 ± 254
B	-	2.87 ± 0.53	694 ± 181
C	1173 ± 176 µ	-	769 ± 254

Comparing both geometries, the hexagonal electrolyte suffers a lower reduction in comparison with the tubular geometry. This may be related to the geometry shape, making that the tubular one suffers a higher reduction because it is more compact than the hexagonal one.

Within this observation, the cathode deposition by using the dip coating methodology was performed on tubular cells. ***Table 4.3*** summarizes the cathode thickness. As it is evident, the deposited cathode increases when the time of immersion inside the cathode paste increases. For this reason, the sample ***1.a*** and ***1.b*** present the thinnest and the thickest cathode layer.

Table 4.3: *Average of the thickness of the cathode deposited by using the dip coating methodology.*

Sample	Thickness of the coating (µm)
1.A	137 ± 69
1.B	149 ± 66
1.C	142 ± 67
1.D	185 ± 58
1.E	187 ± 96

As it is clearly observed in ***Table 4.3***, the specimen ***1.e*** is the best option in terms of thickness to deposit the cathode by using the dip coating technique. But it is important to keep in mind other properties like the porosity of the cathode adhesion with the electrolyte.

4.1.2. Density

On the ***Table 4.4***, the density for each tubular sample is shown. Furthermore, in this table also appear the following parameters: percentage of Ythria to stabilize the zircona, percentage of ceramic particles, T.T. applied, the time of using the material and the time between the printing process and the sintering process.

Table 4.4: *Summary of density results from tubular samples, with all controllable parameters*

Sample	% Y	% Zr_2O	HT[1]	Time A[2]	Time B[3]	ρ (g/cm^3)	ρ/ρ_T (%)[4]
1	8	60	A	0	1	5.35	90.6
2	8	60	B	0	5	5.47	92.7
3	8	70	A	2	1	5.82	98.6
4	8	70	B	2	0	5.79	98.1
5	10	60	A	0	1	4.96	85.6
6	10	60	B	2	2	-	-
7	10	70	A	2	1	-	-
8	10	70	B	0	5	5.35	92.3
9	3	60	A	0	1	5.11	83.8
10	3	60	B	-	-	-	-
11	3	70	A	0	1	5.42	88.8
12	3	70	B	0	2	-	-
13	8	70	A	15	5	5.89	99.9
14	8	70	A	0	5	5.89	99.9
15	8	70	C	15	2	5.79	98.2
16	8	70	C	0	2	5.77	97.8

[1] **T.T (thermal treatment)**: during the Bachelor's project three different treatments were applied. These are widely explained in **section 3.4.**.

[2] **Time A:** Days between the day of preparation the ceramic paste, and the day of use it.

[3] **Time B**: Days between the day of print the sample and the day of put it on the oven.

[4] Theoretical densities used to calculate these percentages are: 3Y-TZP: 6.1 g/cm^3, 8Y-TZP: 5.9 g/cm^3, 10Y-TZP: 5,8g/cm^3 [43].

It is necessary to mention that sample 10 was not even printed, because during the printing process of the sample 9 the material was too fluid, and it was difficult to print. So we decided that after analyze the density for the sample 9 with the same composition as sample 10, was not necessary to print due to the density was not higher than the 90% the theoretical value

The density for the samples 6, 7 and 12 was not able to be determined due to during the sintering process, these specimens broke, mainly due to a non-suitable T.T due to the material employed was 10Y-TZP, which presents a *c*-phase.

For the rest of the specimens, the density obtained for the samples 4 and 5 was higher than 90% as it is evident in ***Table 4.4***. In this sense, the specimens were polished following the procedure explained in ***section 3.7***. However, during this stage, the specimens broke. This phenomena, can been explained because they presented several cracks, and during the polishing process they spread very fast. Moreover, for other specimens, several cracks appeared during the polishing process. Within this observation, new samples were printed, because there had no sense to analyzed the samples that did not break, because the comparison would not be relevant.

The new printed specimens, it was chosen the composition that gave the best density value. It was for samples 3 and 4, which means that the best composition was 8Y-TZP at 70 % wt. of ceramic charge. So four samples were printed with four different conditions;

(*i)* Two of them the T.T. A and C were applied, in order to reduce cracks generated during the sintering process.

(ii) For the other specimens, a different time between preparation and use of ceramic pastes was changed, in particular two different times; 15 and 0 days. ***Table 4.4*** exhibits for samples 13 and 15 presents a time of 15 days between the preparation and use of the pastes, the first one with a T.T. A, while for the other specimen the T.T. applied was C. In the case of samples 14 and 16 have a time of 0 days between the preparation and use of the pastes; the same day of preparation was the same day of use. And as before the first sample a T.T. type A was applied and for the second was a T.T. type B.

Afterwards, the Archimedes method was applied to all the samples to calculate the density. However, for samples 13 and 14, the density was measured by using the helium pycnometer due to by using the Archimedes method the relative density of sample 13 was 100.57% and of the sample 14 was 99.52%. In the end, applying the new technique, the relative density for each sample was 99.95 and 99.86 % for sample 13 and 14, respectively. To sum up, the best relative density was obtained for the next combination: 8Y-TZP at 70%, applying a T.T. type A. As it is mentioned along this paragraph,

there is not much difference between samples 13 and 14, so with all other property results, the decision as to how much time should elapse before printing and before sintering will be made.

On ***Table 4.5,*** the densities of the samples with hexagonal geometries are shown. As we can see the densities are close one to the other, the small difference may be related to the printing process, where small defects appears without our control.

Table 4.5: *Table of density results from hexagonal samples, with all controllable parameters*

Sample	% Y	% Zr_2O	HT	Time A	Time B	ρ (g/cm^3)	ρ/ρ_T (%)
A	8	70	A	0	8	5.79	98.1
B	8	70	A	0	2	5.81	98.4
C	8	70	A	0	2	5.77	97.8

These samples do not reach a density around 99%, because the bases of them are made of a ceramic paste with the idea to generate porosity inside and make the polishing process of the sample easier. The final aim of that is get a really thin layer for the conductivity of the sample. This ceramic paste just has 30 % of ceramic charge and a high Pluronic F-127® charge.

4.1.3. Porosity and defects

Tubular geometry:

From the FESEM microstructure, we can clearly observe that the image presents a nm porosity with a homogeneous circular shape. Furthermore, to study the porosity in tubular samples an image analysis was used to determine the porosity from the FESEM image presented in ***Figure 4.3.*** With this the percentage of porosity in the sample was studied and also the size of this porosity, compiled on ***Table 4.6.***

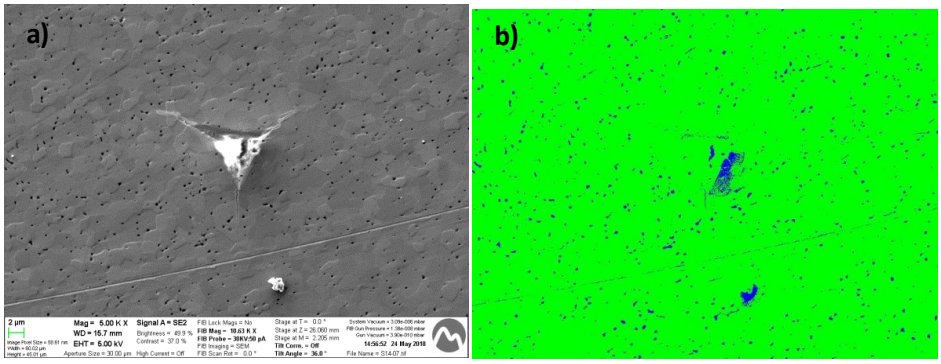

Figure 4.3: *a) The same FESEM image of the sample 14 without treating. B) The FESEM image treated with ImageJ to count the %Porosity.*

Table 4.6: *Average of the percentage of internal porosity*

Sample	13	14
% Porosity	0.34	1.2
Average size	22 ± 2 nm	48 ± 4 nm

First of all, it is necessary to emphasize that the size of the porosity is on the nanometric length scale with a spherical geometry. This porosity may be generated as a consequence of the evacuation of the gelling agent during the isothermal treatment performed during 1 h at 700ºC.

Hexagonal geometry:

Figure 4.4, shows the AFM images (topography and 3D image, ***Figure 4.4.a*** and ***b***, respectively). It shows a close porosity near to the surface of the hexagonal samples. As we can see exists lot of porosity. Furthermore, performing a cross profile it is possible to determine that the maximum high is around 500 nm as it is depicted in ***Figure 4.4.c*****.**

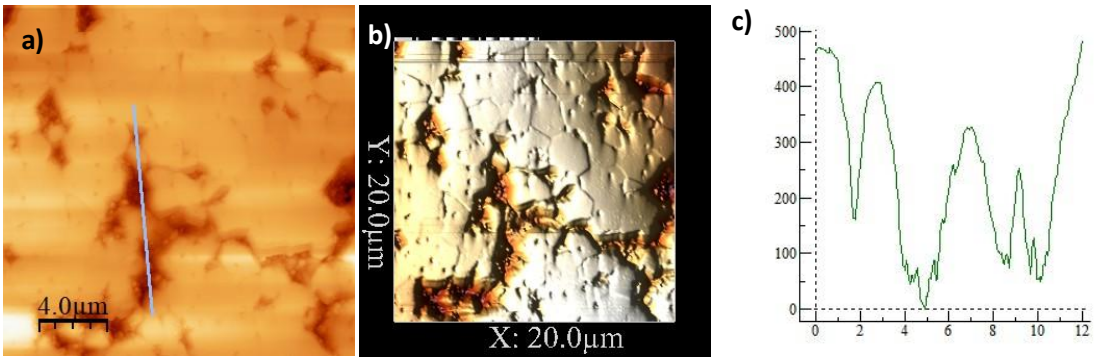

Figure 4.4: *Roughness analysis performed by using the AFM technique. a) topographic image, b) 3D-representation c) topography profile of the porosity of the sample B.*

The AFM technique, will lead to determine how rough is the sample after the polishing process and be able to determine the maximum high as for example presented in ***Figure 4.4.c*** as mentioned above. Furthermore, from the topographic image (***Figure 4.4.a***), it is possible to determine the average roughness for the area observed by AFM, yielding an average roughness value of 48 ± 28 nm. By using FIB and doing a cross-section it is possible to quantify and observe the porosity shape for the printed materials. As it is presented in ***Figure 4.4.a***, the cross-section shows spherical porosity. By combining this FIB image, see ***Figure 4.5***, with an image analysis it is possible to quantify the porosity, being this of around 0.93 %. As it has been presented, the same ceramic paste used to print tubular or hexagonal electrolytes presents a percentage of porosity similar. With this result, it is

possible to conclude that the generation of porosity does not depend on the printed shape if not in the ceramic paste quality, and in particular with the amount of ceramic charge, see ***section 4.1.2.***

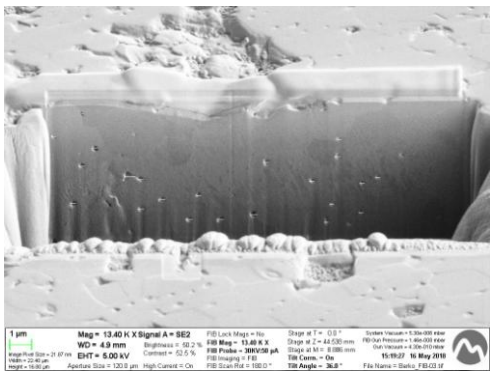

Figure 4.5: *FIB image of the sample B that shows the internal porosity.*

The superficial porosity, see ***Figure 4.5,*** could be explained because of the zirconia material used to print electrolytes presents a higher content of *c*-phase than *t*-phase, see ***section 4.1.5***. This type of phase presents a coarse microstructure with 8Y-TZP grains ranged between 500 – 1000 nm. Furthermore, this phase is harder than the tetragonal and then during the polishing process is possible to induce grains pull-outs, yielding as a result some superficial porosity as we observed in the AFM image, see ***Figure 4.4***.

In conclusion the geometry affects in the size of the porosity but not in the percentage of it. This could explain because both geometries have the same amount of water, but the size is bigger in the hexagonal one because it suffers a lower contraction during the sintering T.T. This implies that the hexagonal samples present a lower chance to suffer a contraction of the structure decreasing the internal porosity.

Coating:

To study the porosity of the deposited coating, a direct image analysis was employed by using the *ImageJ*. In ***Figure 4.6,*** shows the OM micrograph of the interphase between the electrolyte and the cathode. The cathode presents a high porosity, ranged between 10-20 %; this finding is in agreement with the reported in the literature; the cathode must have sufficient porosity to allow gas transport to the reaction sites. The lower limit on porosity is set by mass transport considerations. (The porosity limit may be less critical for mixed conducting materials.) The upper limit is based on consideration of mechanical strength of the component [22].

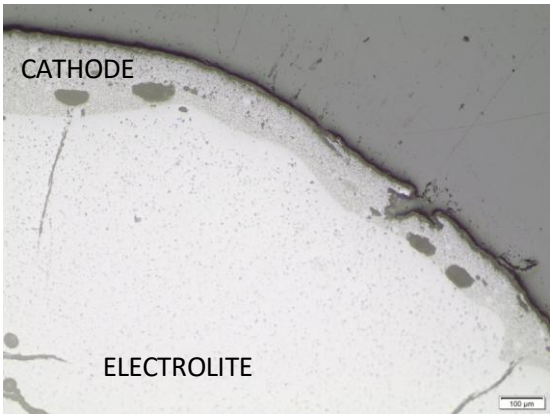

Figure 4.6: *OM micrograph of the interphase between the electrolyte and the cathode.*

4.1.4. Chemical composition

In **Figure 4.7**, the XRP spectrum for the polished surface for the 8Y-TZP printed specimen, see **Figure 4.4**, is presented. In this spectrum the main peaks are indexed, while a secondary peaks ranged between 45 and 75º are not. These peaks may be related to the cubic phase and scarce information related to this material and in particular to this phase is available in the literature.

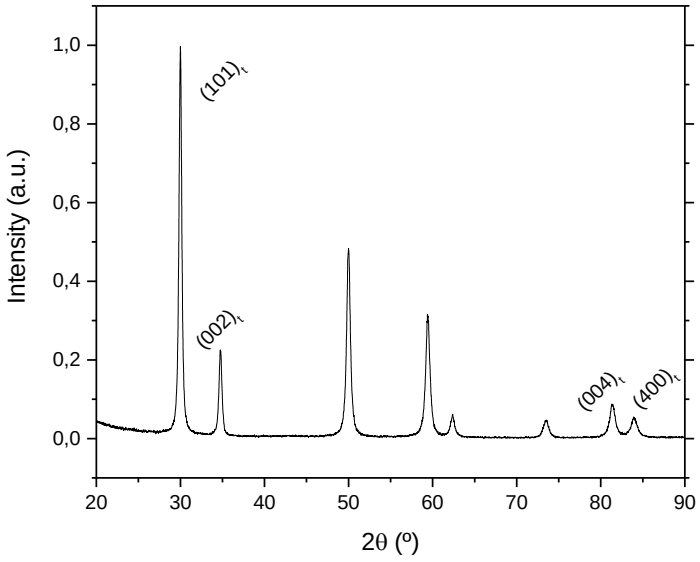

Figure 4.7: *XRD graph of the 8Y-TZP powder from TOSOH, used during the project.*

4.2. Mechanical properties

4.2.1. Nano-Hardness vs. Young Modulus

From the Berkovich indentations values performed at 2000 nm of maximum displacement into surface (or until reach 650 mN of maximum applied load), it is possible to observe the hardness (*H*) and the elastic modulus (*E*) evolution against the displacement into surface for the different specimens performed along this Bachelor's project in order to try to correlate the micromechanical properties with the different processing conditions (see ***Table 3.1, 3.2, 4.4***) as well as for the different geometries.

Furthermore, the micromechanical properties as well as the adherence for the cathode deposited by using the dip coating methodology was also determined.

Tubular geometry:

In the ***Figure 4.8.a*** and ***4.8.b*** are represented the *H* and *E* against the displacement into the surface for the tubular samples 13, 14, 15, 16 (more information related to these specimens can be found in **Table 4.4**), respectively.

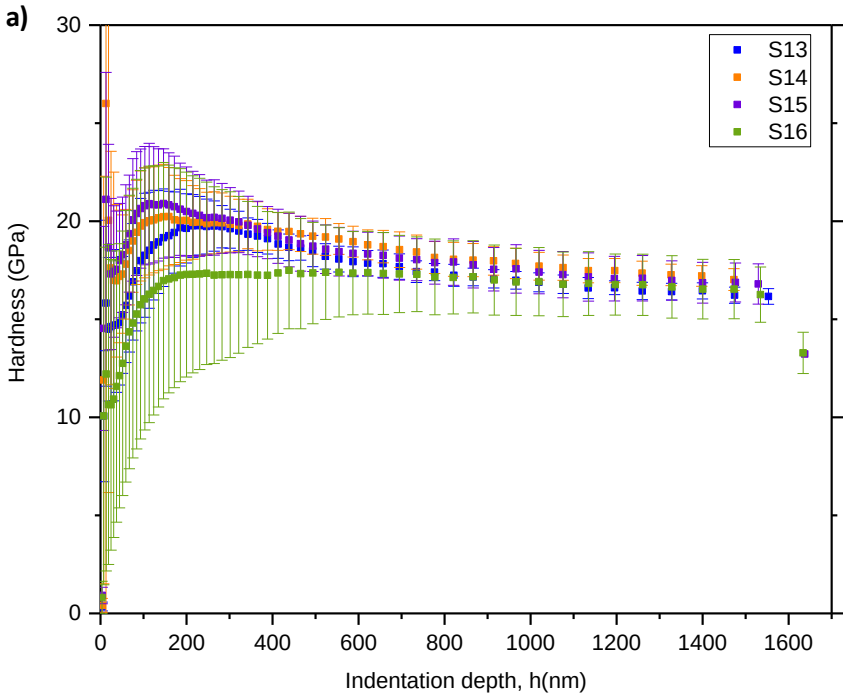

Figure 4.8: *Micromechanical properties for the tubular samples (13, 14, 15, 16) against the displacement into surface. a) Hardness, and b) Elastic modulus.*

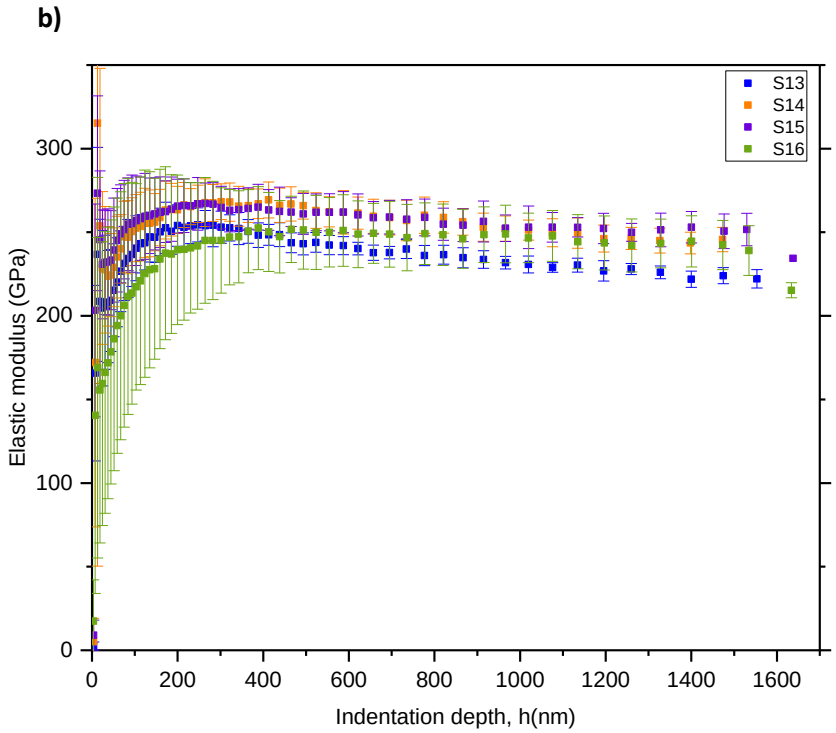

Figure 4.8: *Micromechanical properties for the tubular samples (13, 14, 15, 16) against the displacement into surface. a) Hardness, and b) Elastic modulus. (continuation)*

In ***Figure 4.8a***, two different regions can be appreciated:

(i) For penetrations depths lower than 600 nm, where the *H* does not remain constant with the displacement into surface. In this region, the mechanical parameter is affected by the scale effect (for example superficial roughness, tip defect, etc.).

(ii) On the other hand, when the displacement into surface the *H* value remains stable and more or less constant for all the specimens around 16GPa.

As it is evident in ***Figure 4.8a***, the *H* value does not vary against the displacement into surface for penetrations depth higher than 600 nm, which means that the micromechanical property obtained at this penetration depth represents the 8Y-TZP hardness for the composite.

In ***Figure 4.8b*** a similar effect as mentioned for the *H* curve can be appreciated, The *E* for the different specimens remains constant and ranges between 210 and 250GPa.

Observing in more detail the results represented in ***Figure 4.8***, samples 14 and 15 are slightly hardness and stiffer than the others. This different may be related with the microstructural aspects, like density, as well as different sintering T.T as can be seen in ***Table 4.4***.

Hexagonal geometry:

In ***Figure 4.9.a*** and ***b*** are represented the *H* and *E* trend against the displacement into surface for the hexagonal samples A, B, C. The *H* values for the different specimens with a hexagonal geometry presents an average value of around 15 GPa, which is slightly lower than those reported for the tubular geometry as depicted in ***Figure 4.8.a***. On the other hand, these values present a high standard deviation, which is related to the superficial roughness. As it will be presented in ***section 4.2.2***, the microstructure, this geometry present a grain pull-out generated as a consequence of the *c*-phase present in the 8Y-TZP but mainly due to the printed geometry, which is the main responsible to induce this huge scatter. On ***Figure 4.8.b***, the *E* for the different specimens presents a constant value of 210 GPa, in fair agreement with the value reported for the tubular geometry.

The micromechanical values obtained through the nanoindentation technique and presented in this Bachelor's project due to no information is available in the literature related to the 8Y-TZP sample. However, the *H* values reported here are slightly lower than those reported for the *t*-phase for the 3Y-TZP material [44]. This behaviour is abnormal, due to it is well known the *c*-phase is harder than the *t*- one. In this sense, the results reported here mainly for the hexagonal geometry highlighted the grain pull out induced during the polishing process affects the hardness value. On the other hand, the *E* for the 8Y- and 3Y-TZP are quite similar, as reported Turon *et al.* for the 3Y-TZP specimen [44].

a)

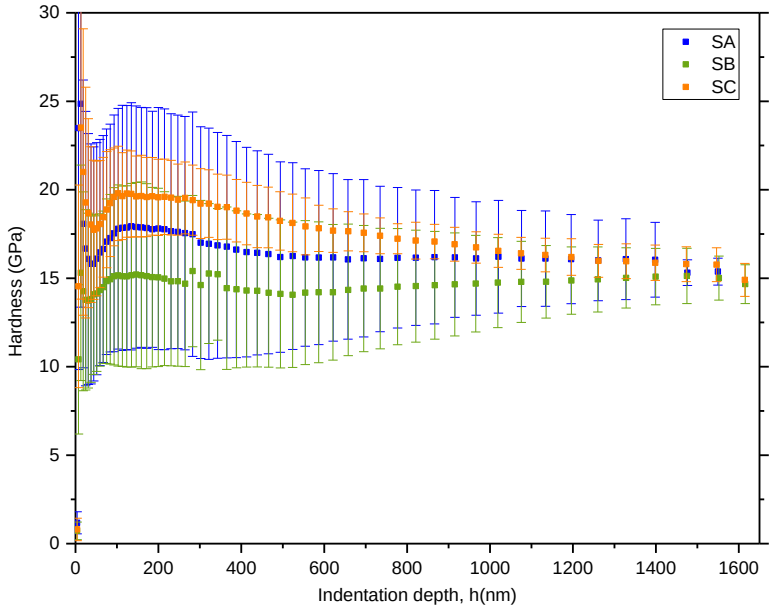

Figure 4.9: *Micromechanical properties for the hexagonal samples (A, B, C) against the displacement into surface a) H, and b) E.*

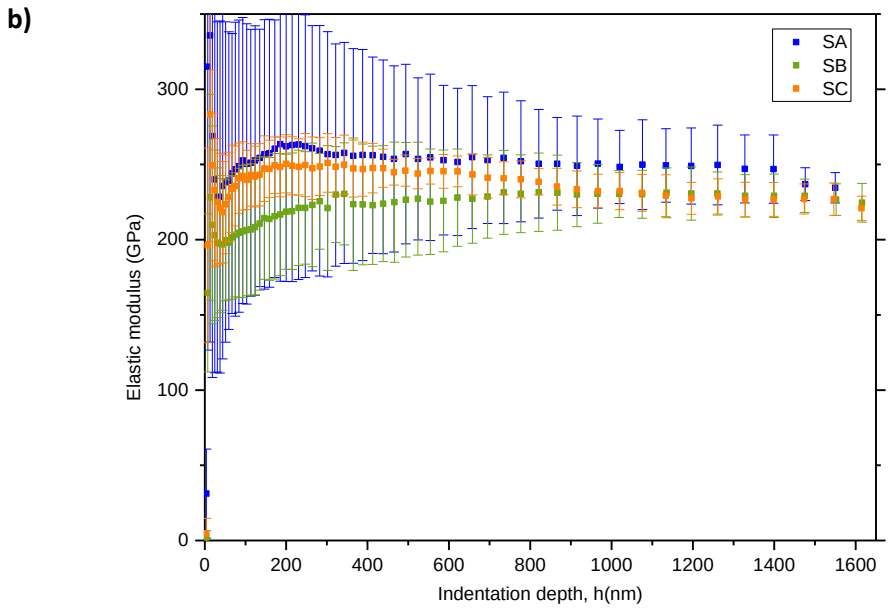

Figure 4.9: *Micromechanical properties for the hexagonal samples (A, B, C) against the displacement into surface a) H, and b) E. (continuation)*

In ***Figure 4.10*** a comparative histogram representation for the micromechanical properties for both geometries investigated in this Bachelor's project are represented for each sample; 13, 14, 15, 16, A, B, C, to see if the geometry affects the investigated properties.

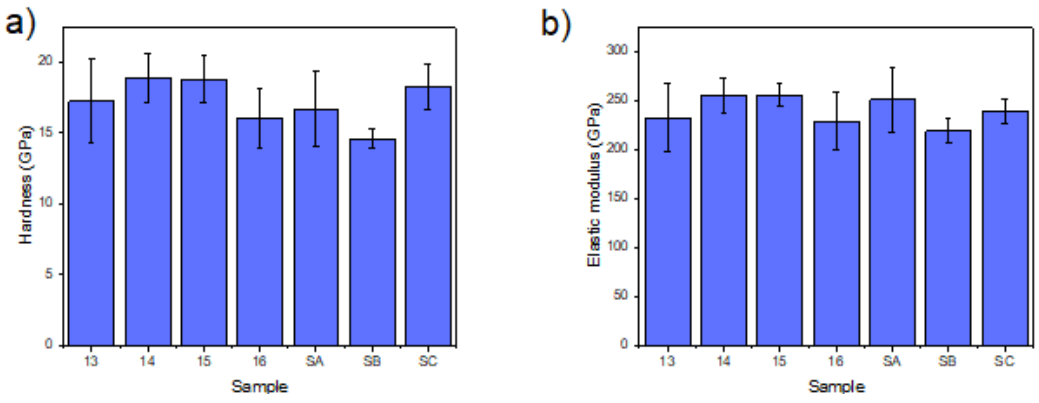

Figure 4.10: *Summary of the micromechanical properties, comparing the two investigated geometries (tubular vs. hexagonal). a) Hardness, and b) Elastic modulus.*

From ***Figure 4.10***, micromechanical properties geometry does not affect the micromechanical properties due to both of them remains more or less constant. The highest value for the *H* is around 18GPa, while the lowest is near 15GPa as it is depicted in ***Figure 4.10.a***, so all of them are similar and in agreement with the values reported with the theoretical value, 17.5GPa [44]. On the other hand,

the E ranges between 225 and 260GPa, being in concordance with the reported value for the 3Y-TZP, 225GPa, as depicted in Refs. [44].

Dip coating:

In the ***Figure 4.11a*** the *H* hardness evolution as a function of the maximum displacement into surface, for the dip coating samples 1.a, b, c, d, and e are represented. As it can be appreciated, all the specimens present a similar hardness of around 12.5GPa, while the specimen S1.c is near 4GPa harder than the others. On the other hand, the *E* values (see ***Figure 4.11.b***) for all the specimens ranges between 180 – 190GPa while the specimen S1.c is 50GPa stiffer than the others.

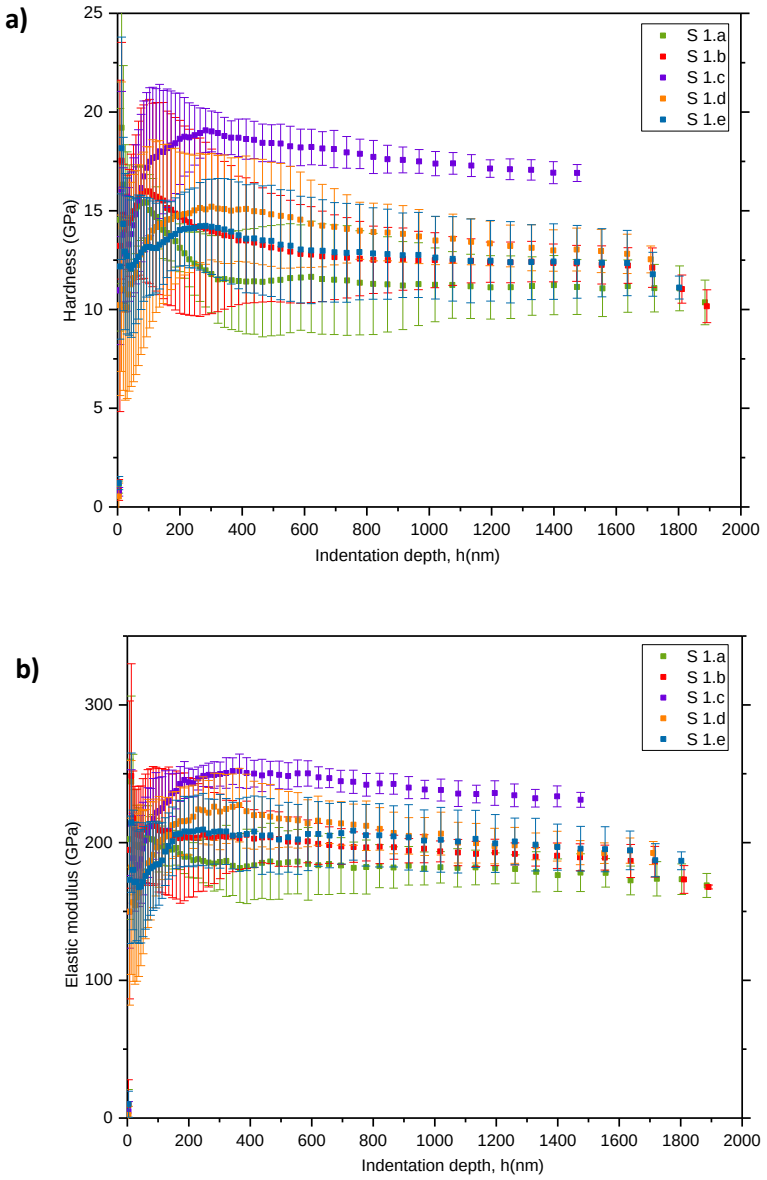

Figure 4.11: *Micromechanical properties for the cathodes deposited on tubular samples (1a, 1b, 1c, 1d and 1e) against the displacement into surface for the a) H, and b) E*

From this representation is possible to conclude that when the deposition time increases the micromechanical properties also increase, that is why sample ***1c*** presents the best micromechanical properties as it is summarized in ***Figure 4.11***. And although the samples ***1d*** and ***1e*** have been immerse more time the process of take them out and put them inside again make that the adhesion of the coating will be worst.

4.2.2. Indentation fracture toughness

In this part a study of the indentation fracture toughness (K_{IC}) of the samples 13, 14 and B was made with the help of the ***equation 4.1*** and the ***Figure 4.12***, giving K_{IC} results are summarized in the ***Table 4.7***.

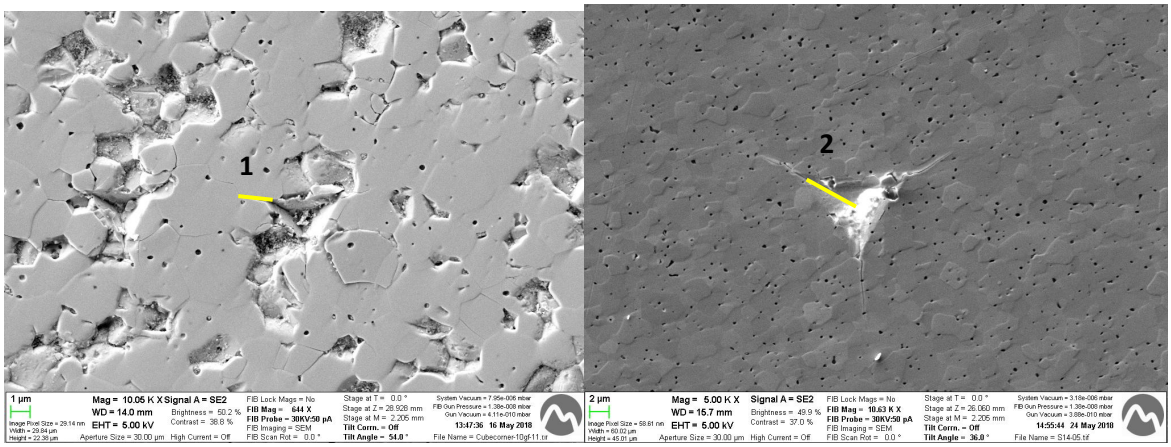

Figure 4.12: *FESEM images of the cube corner nanoindentation imprints. a) Residual imprint done on specimen B at 10gf , and b) Image of the Berkovich indentation on sample 14.*

Table 4.7: *Indentation fracture toughness values.*

Sample	13	14	B
K_{IC} (MPa·√m)	4.38	3.39	3.03

Using the *ImageJ* software, the crack length where measured. Afterwards, the ***equation 4.1*** was used in order to determine the indentation fracture toughness. **Table 4.7** summarizes the K_{IC} values, being the value for the sample 13 higher while the worst one obtained for the sample B. This could be related to the relative density, the sample 13 has the highest one while the sample B that has the lowest relative density, this finding highlight that the microstructural parameters strongly affects the K_{IC}.

4.2.3. Cathode adhesion

To see if the coating has a good adhesion to the electrolyte to have a good performance of the SOFC, a nanoscratch test was made. In the ***Figure 4.13*** the scratch track can be observe. The adhesion tests were performed only on sample ***1.c***, because it presents the best micromechanical properties in terms of *H* and *E* as summarized in **section *4.2.1***.

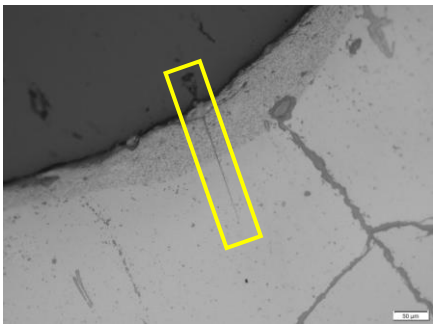

Figure 4.13: *OM image of the nanoscratch on sample 1.c.*

As the ***Figure 4.13*** shows that the scratch test is performed through the electrolyte/cathode interface. As it is clearly evident on this image, no residual cracks are induced at the interface after perform the scratch tests, which means that the final specimen present a high adhesion mainly due to a diffusion phenomenon which occurs between both parts. So it can confirm that when a sliding load is applied it will resist. Further tests may be done in order to exactly know what happen between the electrolyte and the cathode interface.

4.2.4. Damage mechanisms

To analyze the damage events, a matrix of 25 residual imprints performed by using Cube-Corner indentations was made. In the ***Figure 4.14***, the matrix is presented with 5 indentations performed per each applied load: 10, 20, 30, 40 and 50 gf (from the bottom to the upper part of the image).

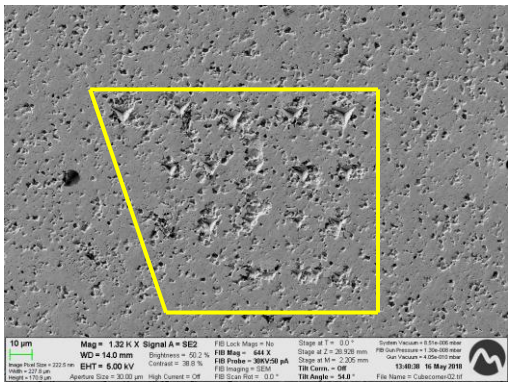

Figure 4.14: *FESEM image of the array of imprints performed for the cube-corner indentations at different applied load.*

To evaluate the induced damage of the indentations performed at different applied load, a graph of the load applied on the sample function against the displacement into surface of the sample was made, see ***Figure 4.15***, for the sample 13, to see when the damage appears. The damage appears in form of radial cracks induced at the edges of the residual imprint as it is shown in the FESEM micrographs. Furthermore, several pop-ins are activated during the loading process, see black arrows. So as it is presented in this figure, the lowest applied load, 10 gf, also presents pop-ins in the loading curve. Then, for the higher applied loads, the damage induced will be higher. Within this context, the load-displacement curves obtained by using a cube-corner indenter for the other specimens were obtained at 10 and 20 gf for the other specimens.

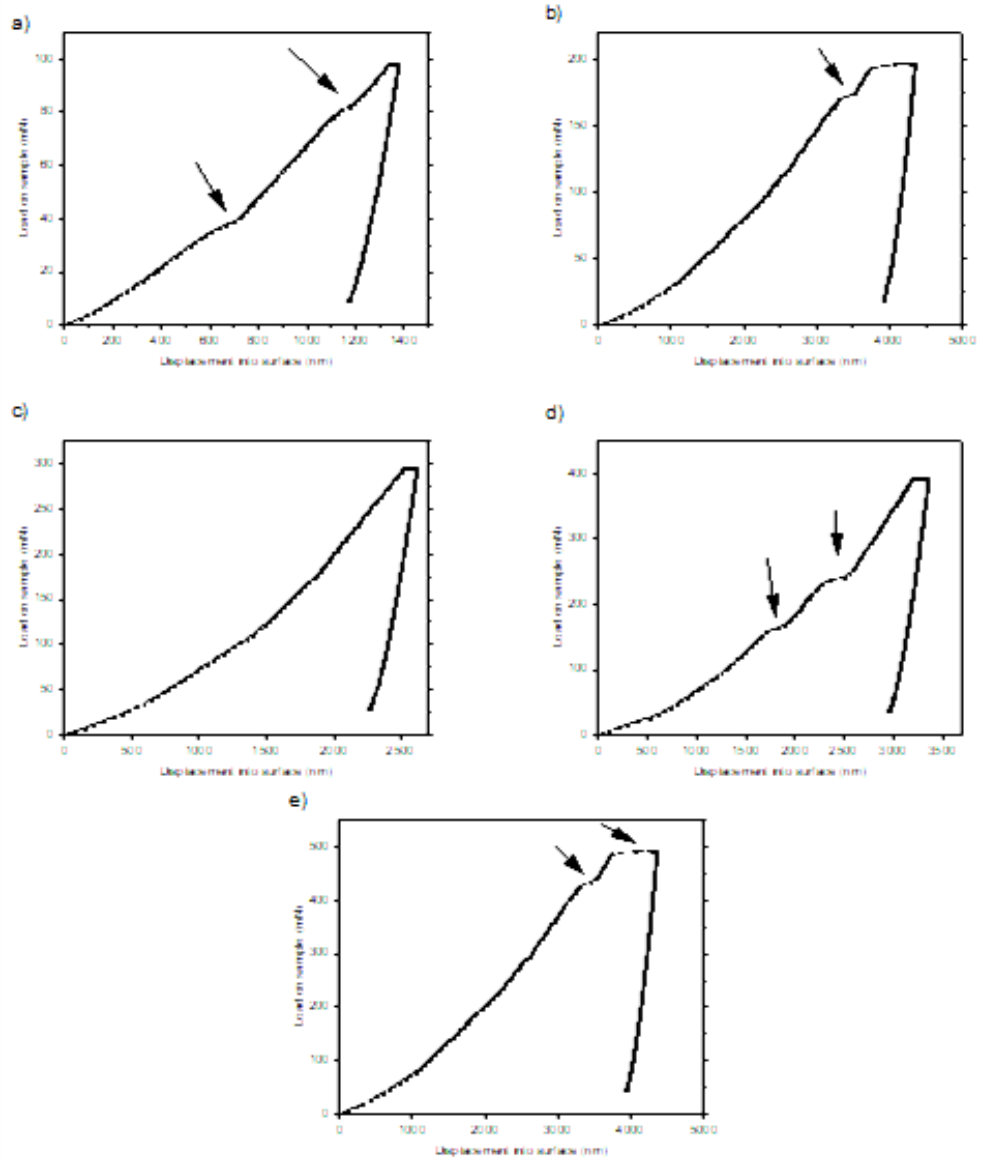

Figure 4.15: *Loading-unloading curves performed with a cube-corner indenter for sample 13 at different applied loads. a) 10 gf, b) 20 gf, c) 30 gf, d) 40 gf and e) 50 gf.*

In ***Figure 4.16*** the loading-unloading curves for the other specimens performed at 10 and 20 gf were represented. With a black arrow the pop-ins induced during the indentation process are represented.

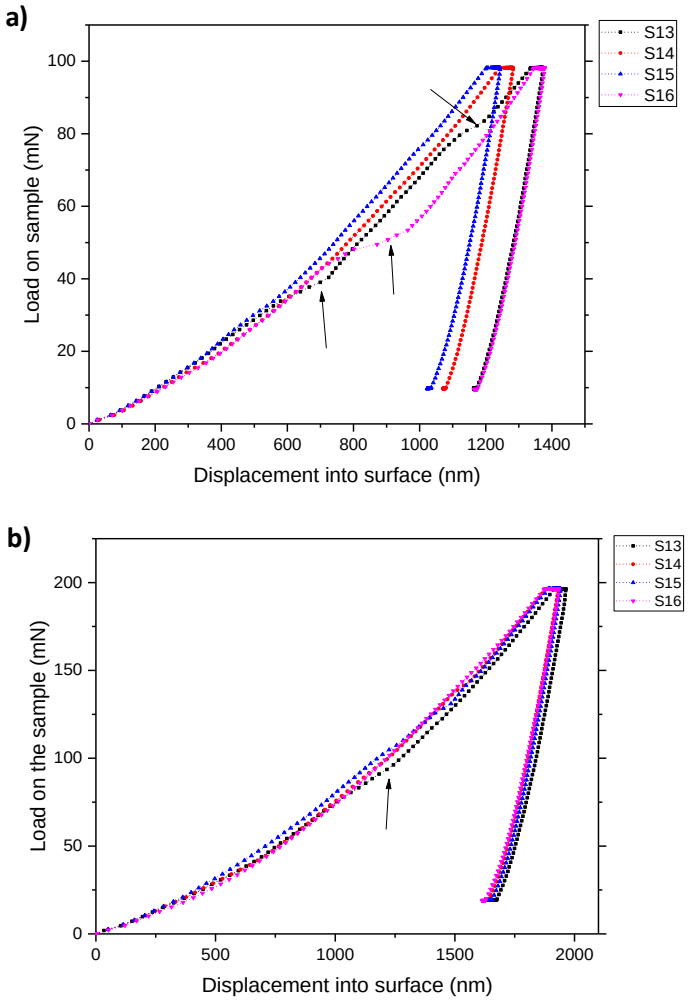

Figure 4.16: *Loading-unloading curves obtained by using the Cube-Corner indenter for the investigated specimens at different applied loads for the tubular samples. a) 10 gf, and b) 20 gf.*

As we can see in the ***Figure 4.16.a*** the samples 13 and 16 suffer pop-ins at an applied load of 10gf, while no pop-ins are evident for the samples 14 and 15 at both investigated loads. As reported in ***equation 3.5***, the indentation fracture toughness depends on the *H* and *E*, being higher for the samples 14 and 15, then is logically that both samples suffer a lower damage in the surface of the sample. So, due to these reasons, both samples do not present pop-ins in the loading curve**.**

For the hexagonal samples the procedure was the same as presented for the tubular images. The matrix of 25 indentations was made on the sample B, taking images of the indentations for the 5 difference loads. And graphing the load applied to the sample as a function of the displacement into

surface for one of the residual indentations done at the investigated load. ***Figure 4.17*** the corresponding graph with the FESEM micrograph are represent.

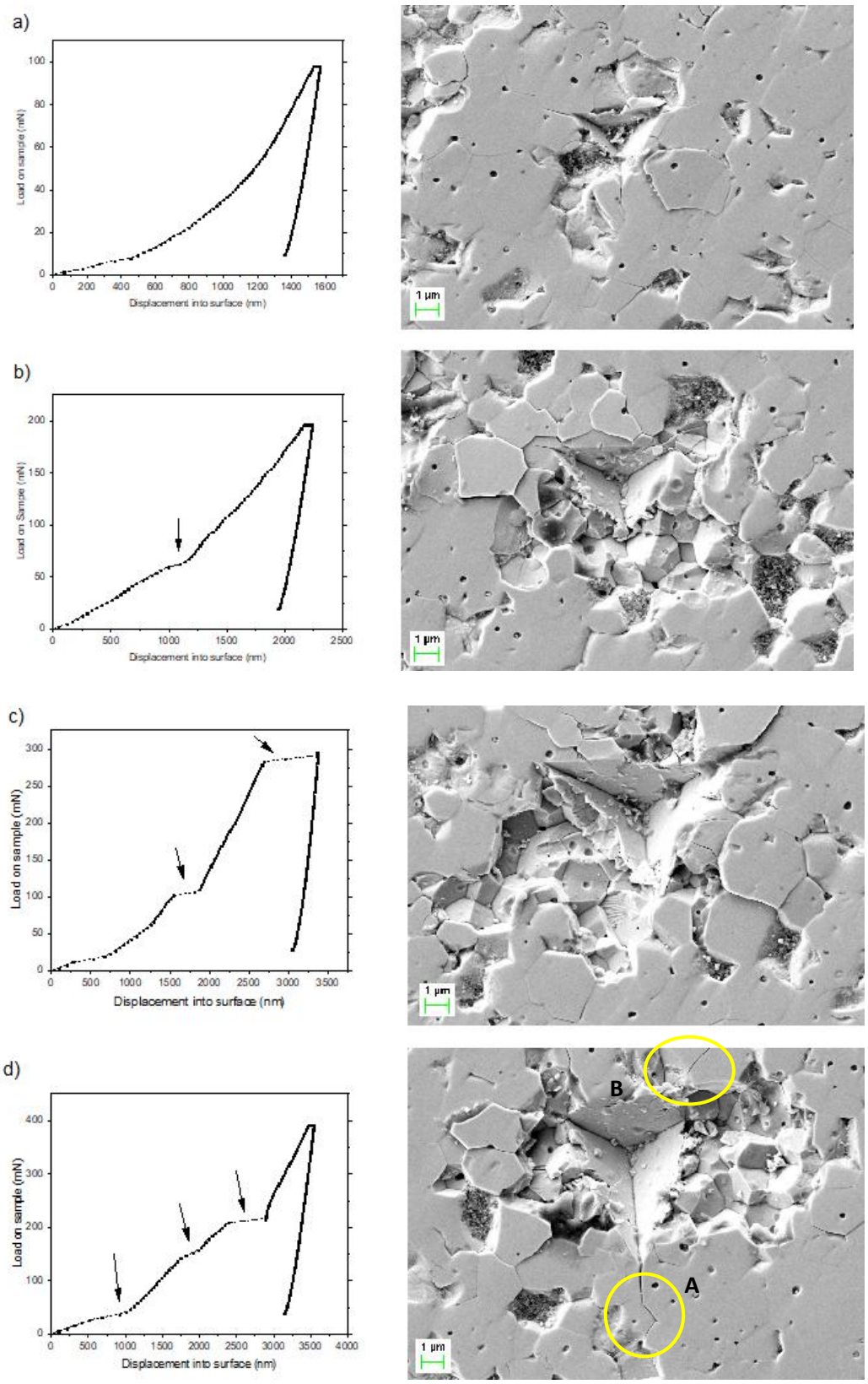

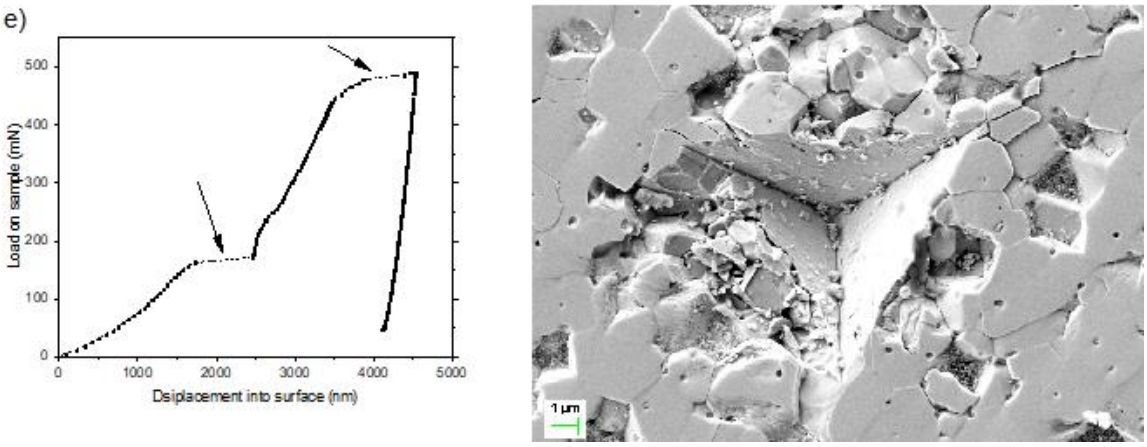

Figure 4.17: *Loading-unloading curve (left hand side) and residual FESEM micrograph for the cube corner imprints performed at different applied loads. a) 10gf, b) 20gf, c) 30gf, d) 40gf and e) 50gf.*

We can see that in this case the pop-in appears in the ***Figure 4.17.b*** with 20gf of load, and when the load increase more pop-in appears and also bigger pop-ins than the previous load. For this reason in the other two samples just the loads of 10 and 20gf were been applied.

Also another interesting thing to remark is the FESEM micrographs presented for the different applied loads, the same fracture dame appear for all the different tests, radial cracks induced at the edges of the residual imprint. These cracks are intergranular (labelled A in ***Figure 4.17.d***) and/or transgranular (labelled B in ***Figure 4.17.d***).

In the ***Figure 4.18*** the loading-unloading curves at 10 and 20 gf for the three hexagonal samples are represented.

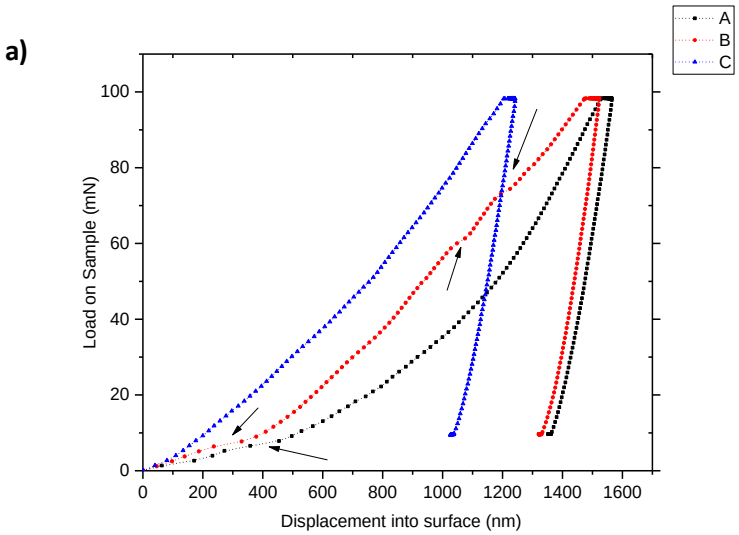

b)

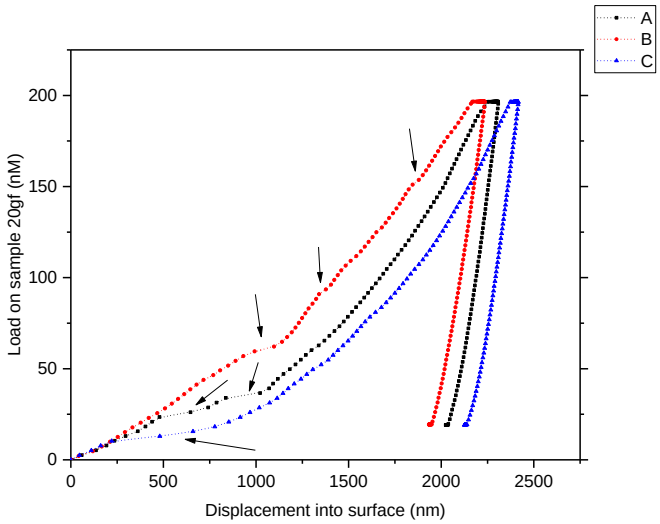

Figure 4.18: *Loading-unloading curve for the cube-corner tests performed on the hexagonal samples at different loads. a) 10gf, and b) 20gf.*

We can see that the sample B is the one that presents more pop-ins in the loading curve, so in consequence it suffers more superficial damage. If we related that result with the mechanical properties we can see that the one that gets the worst micromechanical properties is the one that suffers the higher damage, the sample B. Then, the harder and stiffer material is the brittle one.

4.3. Microstructure vs. elastic modulus

With the help of the ***equation 5.1*** the theoretical values for the *E* determined by using the nanoindentation technique can be write as a function of the percentage of porosity (see ***chapter 4.1.3***) as well as the pore geometry for the 8Y-TZP.

$$E = E_o \cdot \frac{1-P}{1+P\alpha}, with\ \alpha = 1\ and\ \alpha = 0.5 \qquad (5.1)$$

Where *E* is the elastic modulus acquired in the nanoindentation assay, E_o is the theoretical elastic modulus, *P* is the porosity inside the analyzed sample and α is the parameter that indicated which type of geometry gets the porosity.

These values are presented in ***Figure 4.19***. And it is used to see if our experimental values follow this trend and the geometry of the internal porosity of the samples is closed to spherical or lenticular shape. Seeing ***Figure 4.3*** and ***4.5***, the porosity of the sample is closer to a spherical shape than lenticular.

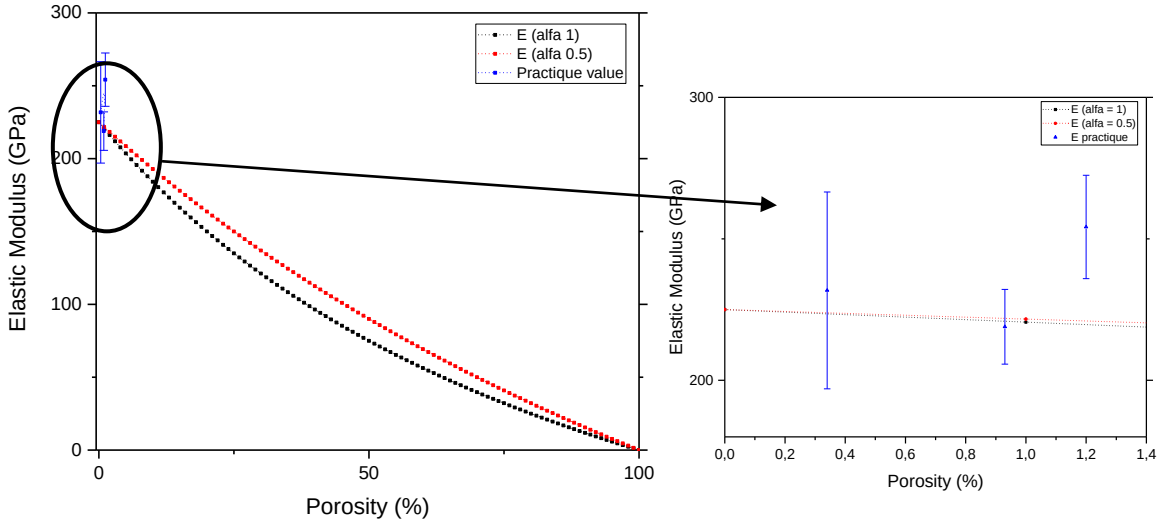

Figure 4.19: *Graphic of the trend of the elastic modulus against the % of porosity. The blue values represent the experimental values determined for the samples 13, 14 and B.*

We can see that our values are closed to the tendency but not inside it. This could be explain because the investigated specimens presents a low porosity, and the porosities of the samples are at the nanometric range making it difficult to measure and calculate. Furthermore, the roughness of the sample affects to these results making that the reason of the huge standard deviation associated to this measurement.

5. Environmental impact analysis

In general terms, in this Bachelor's project, the environmental impact is related to the materials used to prepare the sample and during the processing process as well as the energy associated to perform the T.T., polishing the specimens and the machines employed to microstructural and mechanically characterize the material.

The materials used during the process do not have a high harm for the environment. During the ceramic pastes preparation, all the material was try to be used in order to avoid the generation of waste and leftover products, always trying to make small amounts of ceramic paste.

As far as the processing process, the printing material; syringe, piston and nozzle, during all the process was reused as far as possible, instead of using it as a disposable material. One of the environmental problems was the use of the furnace that has huge energy consumption. Another one was the polishing process. During it many water was used, and the grind paper to polish was to use and throw away. It was generated some waste products, but they were recycled on the correct way.

Finally, when we talk about the characterization process, electrical energy was consumed, but in comparison with the energy used for the furnace, it is not comparable in terms of consume.

6. Conclusions

The results of this final Bachelor's project draw the following conclusions:

(1) In terms of the electrolyte:

From the **geometrical** point of view, the dimensions of the final printed samples are strongly affected by the geometry as follows:

For the *tubular geometry* the final samples suffer a reduction around 30-40%. On the other hand for the *hexagonal geometry* the final samples suffer in the wall thickness a reduction around 10-20%, while the hexagon size a reduction around 30%.

From the **microstructural** and **micromechanical point** of view, the geometry does not affect the final results in terms of density, hardness and elastic modulus being those similar for both printed geometries. In order to get the best microstructural and micromechanical properties the following printed and sintered conditions may take into consideration:

- Work with an hydrogel with a percentage of Pluronic F-127 of 25 wt. %.
- A ceramic paste with a 70 wt. % of ceramic charge of 8Y-TZP.
- Store the specimen during one day before printing at room conditions of temperature and humidity, and giving around 5 days before applying the T.T in order to dehydrate the specimen.
- For the printing process the two most important parameters are: the velocity of printing that it needs to be low, and the infill of 100% to have full dense samples.
- Apply the T.T A.

The printed specimens present a high density, around 99% and in some cases even higher. Furthermore, for these particular cases, the porosity is near 1 % or less, with a porosity size of several tens of nanometers. This parameter is not also affected by the printed geometry. The material used during this project, 8Y-TZP, presents a cubic phase as the XRD spectrum shows. Due to this microstructure, the hardness for this printed material is slightly harder than for the 3Y-TZP.

Also the mechanical properties, *H* and *E*, can be related to the fracture toughness of each sample and with the damage done induced during the test. Within this context, we can conclude that:

- The samples with the highest relative density are the ones that have the highest value of $K_{IC,}$ due to the *H* and *E* are harder and stiffer than the others due to this specimen exhibit less pore density. On the other hand, when a sharp indenter is used in order to induce dame, the loading-unloading curves present several pop-ins which are related to the radial cracks induced at the corners of the residual imprint.

(2) In the terms of the deposited cathode:

The thickness of the deposited cathode depends of the deposition time and also the total amount the electrolyte is immersed inside the solution.

The deposited coated presents a bimodal porosity, coarse and ultra fine, ranged between tens of micrometers up to the nanometric scale, respectively. This layer presents a porosity ranged between 10 to 20 %.

The mechanical and the tribological properties in terms of hardness, elastic modulus and the adhesion, respectively are in close agreement with the data reported in the literature.

So to sum up, this Bachelor's project shows that is possible to get printed parts of a SOFC, getting the same density as well as the mechanical properties than the traditional techniques. So it is possible to combine advanced techniques with an advanced application as the SOFCs are.

7. Budget and financial analysis

Table 7.1: *Summary of the consumables employed in this Bachelor's project.*

CONSUMABLES			
Product	**Quantity**	**Cost/ud.**	**Cost**
Pluronic F-127	0.40 Kg	190 €/Kg	76 €
3Y-TZP	0.1 Kg	125 €/Kg	12.50 €
8Y-TZP	0.3 Kg	125 €/Kg	37.50 €
10Y-TZP	0.1 Kg	125 €/Kg	12.50 €
LSM	0.04 Kg	4.9 €/g	196 €
Distilled water	1Kg	0.7 €/Kg	0.70 €
Grinding paper P120	5	0.8 €/un.	4 €
Grinding paper P320	5	0.8 €/un.	4 €
Grinding paper P600	5	0.8 €/un.	4 €
Grinding paper P1200	5	0.8 €/un.	4 €
Cloth MD-Dac	2	53 €/un.	106 €
Cloth MD-Nap	1	75 €/un.	75 €
Diamond suspension 6µm	0.1 L	83 €/L	8.30 €
Diamond suspension 3µm	0.1 L	75 €/L	7.50 €
Colloidal silica suspension	0.1 L	150 €/L	15 €
Acetone	0.2 L	8 €/L	1.60 €
Epoxy resin	0.1 L	11.16 €/L	1.12 €
SUBTOTAL:			**565.72 €**

Table 7.2: *Summary of the equipment employed in this Bachelor's project.*

EQUIPMENT			
Equip	**Quantity**	**Cost/ud.**	**Cost**
Balance	5 h	10.3 €/h	51.50 €
SpeedMixer	5 h	5 €/h	25 €
3D Printer	40 h	12.4 €/h	500 €
Nabathern Furnace	140 h	12.4 €/h	1736 €
Polisher LaboPol-5	20 h	12.4 €/h	248 €
OM	10 h	13.45€/h	134.50 €
Nanoidenter	20 h	60 €/h	1200 €
SEM-FIB	3 h	150 €/h	450 €
AFM	2 h	30 €/h	60 €
XRD	1 measure	22.44 €	22.44 €
Magnify lent	10 h	7 €/h	70 €
SUBTOTAL:			**4497.44 €**

Table 7.3: *Summary of the personal costs employed to conduct this Bachelor's project.*

COST OF SUPPORT ENGINEERING			
Concept	Quantity	Cost/ud.	Cost
Support technician	20 h	40 €/h	800 €
Supervisor	25 h	50 €/h	1250 €
SUBTOTAL:			**2050 €**

Table 7.4: *Summary of the cost of engineering by the designer.*

COST OF ENGINEERING BY THE DESIGNER			
Concept	**Quantity**	**Cost/ud.**	**Cost**
Sample preparation	200 h	24.8 €/h	4960 €
Sample Characterization	50 h	24.8 €/h	1240 €
Search for information	100 h	24.8 €/h	2480 €
Analysis results	120 h	24.8 €/h	2976 €
Memory development	380 h	24.8 €/h	9424 €
SUBTOTAL:			**21080 €**

Table 7.5: *Summary table of the total cost of the project.*

TOTAL COST OF THE PROJECT	
Concept	**Cost**
Total cost associated with consumables	565.72 €
Total cost associated with the sample characterisation	4497.44 €
Total cost associated with the engineering	21080 €
Total cost associated with support engineering	2050 €
TOTAL:	28193 €
IVA (21 %):	5920.56 €
TOTAL + IVA:	**34113.56 €**

8. Bibliography:

[1]:K. Satish Prakash, et al., *Additive Manufacturing Techniques in Manufacturing – An Overview,* Materials Today: Proceedings 5 (2018) 3873.

[2]: H. Yin, et al., *Fabrication of Ceramic Photonic Crystals with Diamond Structure for Microwave Applications,* J. Am. Ceram. Soc., 87 (2004) 598.

[3]: A. Woesz, et al., *Towards Bone Replacement Materials from Calcium Phosphates Via Rapid Prototyping and Ceramic Gelcasting,* Mater. Sci. Eng., C, 25 (2005) 181.

[4]: C. Bergmann, et al., *3D Printing of Bone Substitute Implants Using Calcium Phosphate and Bioactive Glasses*, J. Eur. Ceram. Soc., 30 (2010) 2563.

[5]: U. Klammert, et al., *Cytocompatibility of Brushite and Monetite Cell Culture Scaffolds Made by Three-Dimensional Powder Printing*, Acta Biomater., 5 (2009) 727.

[6]: G. A. Fielding, et al., *Effects of Silica and Zinc Oxide Doping on Mechanical and Biological Properties of 3D Printed Tricalcium Phosphate Tissue Engineering Scaffolds*, Dent. Mater., 28 (2012) 113.

[7]: J. Suwanprateeb, et al*., Mechanical and In Vitro Performance of Apatite–Wollastonite Glass Ceramic Reinforced Hydroxyapatite Composite Fabricated by 3D-Printing,* J. Mater. Sci. Mater. Med., 20 (2009) 1281.

[8]: F.-H. Liu, et al., *Selective Laser Sintering of a Hydroxyapatite-Silica Scaffold on Cultured MG63 Osteoblasts In Vitro,* Int. J. Precis. Eng. Manuf., 13 (2012) 439.

[9]: R. L. Simpson, et al., *Development of a 95/5 Poly(L-Lactide-co-Glyco- lide)/Hydroxylapatite and b-Tricalcium Phosphate Scaffold as Bone Replacement Material Via Selective Laser Sintering*, J. Biomed. Mater. Res. B Appl. Biomater., 84B (2008) 17.

[10]: R. I. Tomov, et al., *Direct Ceramic Inkjet Printing of Yttria-Stabilized Zirconia Electrolyte Layers for Anode-Supported Solid Oxide Fuel Cells,* J. Power Sources, 195 (2010) 7160.

[11]: E. Ozkol, et al., *An Experimental Analysis of the Influence of the Ink Properties on the Drop Formation for Direct Thermal Inkjet Printing of High Solid Content Aqueous 3Y-TZP Suspensions,* J. Eur. Ceram. Soc., 30 (2010) 1669.

[12]: J. Cesarano, et al., and Inventor: Sandia Corporation, Assignee, *Freeforming Objects with Low-Binder Slurry*; US Patent 6027326 A; February 22; US6027326 A, 2000.

[13]: J. A. Lewis, et al., *Direct Ink Writing of Three-Dimensional Ceramic Structures,* J. Am. Ceram. Soc., 89 (2006) 3599.

[14]: Q. Fu, et al., *Direct Ink Writing of Highly Porous and Strong Glass Scaffolds for Load-Bearing Bone Defects Repair and Regeneration*, Acta Biomater., 7 (2011) 3547.

[15]: J. E. Smay, et al., *Directed Colloidal Assembly of Linear and Annular Lead Zirconate Titanate Arrays,* J. Am. Ceram. Soc., 87 (2004) 293.

[16]: J. E. Smay, et al., *Direct Writing of Dielectric Ceramics and Base Metal Electrodes,* Int. J. Appl. Ceram. Technol., 4 (2007) 47.

[17]: Stein A, *Disadvantages of 3D printers*. eHow TECH. Visited: 03/03/18. Available: http://www.ehow.com/facts_7652991_disadvantages-3d-printers.html.

[18] : S. Bose, et al., *Additive manufacturing of biomaterials,* Progress in Materials Science, 93 (2018) 45.

[19]: Assembly, *Additive manufacturing Takes Off in Aerospace Industry,*Visited : 04/23/18. Available: https://www.assemblymag.com/articles/93176-additive-manufacturing-takes-off-in-aerospace-industry

[20] : A. Bandyopadhyay, et al., *Additive manufacturing of multi-material structures,* Materials Science & Engineering R, 129 (2018) 1.

[21]: S. Masciandaro, et al., *Three-dimensional printed yttria-stabilized zirconia self-supported electrolytes for solid oxide fuel cell applications,* Journal of the European Ceramic Society 5 (2017) 512.

[22]: N. Q. Minh, et al., *Science and technology of ceramic fuel cells*. Elsevier. 1995. ISBN: 44489568X. (Pages: 1, 2, 3, 4, 6, 8, 75, 118, 149, 160, 161)

[23]: Microgrid Knowledge, *The rise of Fuel Cell Microgrids: Special Report,* Visited: 04/23/2018. Available: https://microgridknowledge.com/fuel-cell-microgrids-fuelcell-energy/

[24]: *Crystal structure,* Visited: 04/18/18. Available: https://archive.cnx.org/contents/e90d5161-66b0-4214-bd6c-9f1d20a35bae@10/crystal-structure

[25]: Delaware Mineralogical Society, *The colours of Fluorite,* Visited: 04/18/18. Available: http://www.delminsociety.net/motm/motm_mar2007.shtml

[26]: M. S. H. Akash, et al., *Natural and Synthetic Polymers as Drug Carriers for Delivery of Therapeutic Proteins,* Polymers Reviews 6 (2015) 1.

[27]: Y. Maazouz, et al., *Self-hardening and thermoresponsive alpha tricalcium phosphate/pluronic pastes*, Acta Biomaterialia (2016), doi: http://dx.doi.org/ 10.1016/j.actbio.2016.11.043

[28]: H. Geng, et al., *Sustained release of VEGF from PLGA nanoparticles embedded thermo-sensitive hydrogel in full-thickness porcine bladder acellular matrix,* Nanoscale Research Letters 6 (2011) 312.

[29]: M. Asadikiya, et al., *Phase diagram for nano-yttria-stabilized zirconia system,* Royal Society of chemistry 6 (2016) 17438.

[30]: E. Feilden et al., *Robocasting of structural ceramic parts with hydrogel inks*, Journal of the European Ceramic Society 36 (2016) 2525.

[31]: Y. Fernández, et al., *Guia del Usuario – P1503023 – UPC – BCN3D+ Dual Paste,* Fundació CIM (BarcelonaTech) (2015).

[32]: R. A. Wilson, et al., *Introduction to Scanning Probe Microscopy (SPM): Basic Theory Atomic Force Microscopy (AFM),* Creative Commons Attribution-Noncomercial-Share Alike, vol. 2 (2006).

[33]:L. Lianquing, et al., *Chapter 4-Atomic Force Microscope-Based Nanorobotic system for Nanoassembly,* in Nano Optoelectronic Sensors and Devices, ed. Oxford: William Andrew Publishing, (2012) 51.

[34]: H. Yao, et al., *FORMATEX-Modern Research and Educational Topics in Microscopy,* PhD Thesis, School of Materials Science, UPC University, Barcelona (2013).

[35]:B. S. Majumdar, et al., *FE-SEM Principle,* New Mexico Tech-Materials Department, New Mexico, US (2009).

[36]:P. R. Munroe, et al., *The application of focused ion beam microscopy in the material sciences,* Materials characterization 60 (2009) 2.

[37]: *Micro/Nano Master Fabrication Technology.* Nano Fabrication and Micro Optics National Research Laboratory. Visited (05/21/18). Available: http://nanomolding.yonsei.ac.kr/research/2_2.htm

[38]: Surface-Tec, *Nanoidenter Tip,* Visited: 05/21/18. Available: http://www.surface-tec.com/nanotips.php

[39]: J. J. Roa, et al., *Mechanical characterization at Nanometric Scale of Ceramic Superconductor Composites,* in Nanotechnology: Nanofabrication, Pattering and Self Assembly, C. J. Dixon and O. W. Curtines, Eds., ed: Nova Science Publishers (2010) 151.

[40]: J. J. Roa, et al., *Nanohardness and Young's modulus of YBCO samples textured by the Bridgman technique,* Nanotechnology 18 (2007) 385701.

[41]: M. Laugier, *New formula for indentation toughness in ceramics,* Journal of materials science letters 6 (1987) 355.

[42]: *Examining Interfacial Adhesion of Biomedical Coatings*. Paint & Coatings Industry. Visited: 05/21/18. Available: https://www.pcimag.com/articles/100920-examining-interfacial-adhesion-of-biomedical-coatings

[43]: Tosoh, *Zirconia Brochure,* Visited: 05/22/18. Avaliable: http://www.eskens.com/wp-content/uploads/2014/05/ZIRCONIA-BROCHURE.pdf

[44]: M. Turon-Vinas, et al*.,* Ceramics International. 41 (2015) 14988.

9. Annexe:

9.1. Annexe A: Data sheets

9.1.1. Annexe A.1: Pluronic F-127 Sigma Aldrich

SIGMA-ALDRICH®

sigma-aldrich.com

3050 Spruce Street, Saint Louis, MO 63103, USA
Website: www.sigmaaldrich.com
Email USA: techserv@sial.com
Outside USA: eurtechserv@sial.com

Product Specification

Product Name:
Pluronic® F-127 – powder, BioReagent, suitable for cell culture

Product Number:	**P2443**
CAS Number:	9003-11-6
MDL:	MFCD00082049

TEST	Specification
Appearance (Color)	White
Appearance (Form)	Powder
Solubility (Color)	Colorless
Solubility (Turbidity) 50 mg/mL, H2O, at less than 10 deg C	Clear
pH (2.5% solution)	6.0 - 7.0
Moisture Content	≤ 0.75 %
Cell Culture Test	Pass
Recommended Retest Period 2 Years	----------
Note Pluronic is a registered trademark of BASF SE.	----------

Specification: PRD.1.ZQ5.10000051983

9.1.2. Annexe A.2: Zirconia Tosoh:

Powder Characteristics and Properties

	TZ-3Y-E (TZ-3YB-E)	TZ-3YS-E (TZ-3YSB-E) (TZ-3YSB-C)	TZ-4Y	TZ-6Y	TZ-8Y	TZ-8YS (TZ-8YSB)	TZ-10YS	TZ-3Y20A (TZ-3Y20AB)	TZ-0
Y_2O_3 (mol%)	3	3	4	6	8	8	10	3	0
Actual Particle Size (μm)	0.04 (40nm)	0.09 (90nm)	0.04 (40nm)			0.09 (90nm)		–	0.04 (40nm)

Powder Characteristics

Y_2O_3 (wt%)	5.2 ± 0.5		7.0 ± 0.6	10.3 ± 0.6	13.3 ± 0.6		15.9 ± 0.7	3.9 ± 0.3	–
Al_2O_3 (wt%)	0.1 ~ 0.4		≦ 0.1					18 ~ 22	≦ 0.1
SiO_2 (wt%)	≦ 0.02								
Fe_2O_3 (wt%)	≦ 0.01								
Na_2O (wt%)	≦ 0.04		≦ 0.06	≦ 0.12				≦ 0.04	≦ 0.04
Specific Surface Area (m^2/g)	16 ± 3	7 ± 2	16 ± 3			7 ± 2	6 ± 2	15 ± 3	14 ± 3

Typical Properties of Sintered Body

Density (g/cm^3)	6.05	6.05	6.02	5.90	5.80	5.50	–
Bending Strength R.T. (MPa)*1	1200	1000	500	300	200	2000 (HIPing)	–
Hardness(Hv10)*2	1250					1400	–

*1 : JIS R1601(3-point bending test) *2 : JIS R1610 (Loads : 98.07N)

9.1.3. Annexe A.3: LSM Sigma Aldrich:

SIGMA-ALDRICH®

sigma-aldrich.com

3050 Spruce Street, Saint Louis, MO 63103, USA
Website: www.sigmaaldrich.com
Email USA: techserv@sial.com
Outside USA: eurtechserv@sial.com

Product Specification

Product Name:
Lanthanum gallate, strontium and magnesium doped - powder, 0.3-0.6 µm, 99% trace rare earth metals basis

Product Number: **757357**
CAS Number: 165900-07-2

$La_{0.8}Sr_{0.2}Ga_{0.8}Mg_{0.2}O_3$

Formula: La0.8Sr0.2Ga0.8Mg0.2O3
Formula Weight: 237.29 g/mol

TEST	Specification
Appearance (Color)	White to Light Brown
Appearance (Form)	Powder
X-Ray Diffraction	Conforms to Structure
Surface Area	4 - 8 m2/g
Particle Size (µm) (d50)	0.4 - 0.8
Purity 99% Based On Rare Earth Analysis	Meets Requirements
Trace Rare Earth Analysis	≤ 20000.0 ppm

Specification: PRD.1.ZQ5.10000031358

9.1.4. Annexe A.4: Synolite 0328-A-1:

Product Data Sheet

DSM
BRIGHT SCIENCE. BRIGHTER LIVING.

Synolite 0328-A-1

Applications
Synolite 0328-A-1 is recommended for the production of water clear castings and encapsulations.

Principal properties
Synolite 0328-A-1 is a pre-accelerated low reactivity orthophthalic acid based resin with a very gradual cure. The product has a low peak exotherm combined with a low polymerisation shrinkage and high brilliance after polymerisation. This resin is UV-light stabilised.

Product specifications upon delivery

Property	Range	Unit	TM
Viscosity, 23°C	360 - 620	mPa.s	2013
Colour, APHA	max. 70	-	2017
Solids content, IR	61.5 - 64.5	%	2033
Refractive index, 23°C	1.545 - 1.547	-	2150
Appearance	clear	-	2265
Colour	blue	-	
Water content	Max. 1000	ppm	2350
Acid value, as such	12 - 18	mg KOH/g	2401
Gel time from 25 to 35°C	19 - 23	minutes	2625
Cure time from 25°C to peak	42 - 57	minutes	2625
Peak temperature	40 - 50	°C	2625

Remarks:
TM 2013: Z2/100s^{-1}/23°C
TM 2625: 1.0 g Butanox M50 (Akzo) in 100 g resins

Other data

Property	Value	Unit	TM
Density, 20°C	appr. 1100	kg/m³	2160
Flash point	appr. 33	°C	2800
Stability, no init., dark, 25°C	6	months	-

Typical physical properties of cast unfilled resin

Property	Value	Unit	TM
Density, 20 °C	appr. 1100	kg/m³	2160
Volume shrinkage	6,1	%	-
Tensile strength	56	MPa	ISO 527-2
Elongation at break	1,6	%	ISO 527-2
Flexural strength	83	MPa	ISO 178
Modulus of elasticity in tension	4,1	GPa	ISO 178
Heat deflection temperature (HDT)	55	°C	ISO 75-A
Barcol hardness	40-45	Barcol	GYZJ 934-1
Martens temperature	49	°C	DIN 53548

Guidelines before use
Before use, the resin should be conditioned at a well defined, application dependant temperature (usually 15°C minimum for a MEKP cure). Stir the product before blending.

Storage guidelines
The resin should be stored indoors in the original, unopened and undamaged packaging, in a dry place at temperatures between 5°C and 30°C.
Shelf life is reduced at higher temperatures and the properties of the resin might change during storage. The shelf life of styrene containing unsaturated polyesters will be significantly reduced when exposed to light. Store in dark and in 100% light tight containers only.

Material Safety
A material safety data sheet for the product is available on request.

Test methods
Test methods (TM) referred to in the table(s) are available on request

11.0

9.2. Annexe B: Software

9.2.1. Annex B.1: Slic3r

Available: http://slic3r.org/, visited 30/05/2018

Slic3r is the tool you need to convert a 3D model into printing instructions for your 3D printer. It cuts the model into horizontal slices (layers), generates toolpaths to fill them and calculates the amount of material to be extruded.

This free program is used in the university to generate the *Gcode.* Files directly used in the 3D-printing machine. It gives the possibility of modify the main printing parameters: infill of the layer, the geometry of the infill and the printing velocity. Also this program needs some inputs parameters for print like the size of the nozzle and the size of the printing bed.

In the following part, a brief explanation of the inputs used during this Bachelor's project will be presented:

1. First of all is important to export de *STL.* file and go to *File* → *Export Conf Bundle* → and select the file of the extruder that you are going to use.
2. The first parameter that you need to modify is the *Printing Settings* (***Figure B.1***). In ***Figure B.2 a*** are presented all the parameters.
    - **Layers and perimeters:**
        - *Layer height: h* = Diameter of the nozzle - (0.1*diameter of the nozzle) in the both options.
        - *Vertical shells* (for perimeters): *perimeter* = 1, and choose *Spiral vase*.
        - *Quality* (for perimeters): choose all the four options
    - **Infill:**
        - *Infill:* the *Fill density* for this Bachelor's project is 100% for tubular geometry and 0% for the hexagonal geometry (perimeter). The *Fill pattern* and *Top/bottom fill pattern* → *Rectilinear.*
        - *Advanced:* In this option is just needed to modify the *Fill angle* in the tubular geometry every layer rotating it 90º, to get better mechanical properties.
    - **Speed:**
        - *Speed for print moves:* for all options reduce the time to *5 mm/s*. Except for *External perimeters, Support material* and *Support material interface*, in this case is important to keep the default values.
        - *Speed for non-print moves*: Reduce the velocity to 25 mm/s.
    - **Skirt and brim:**

- *Skirt: Loops* = 1.

3. The following parameter is the *Printer Settings* (***Figure B.1***). In the ***Figure B.2 b*** are presented all the parameters.
    - **General:**
        - *Size and coordinates:*
            - *Bed size: x* = 110; *y* = 240 mm.
            - *Print center: x* = 55; *y* = 120 mm.
            - *Z offset :* In this option for every layer you need to add the height of the layer.
    - **Extruder 1:**
        - *Size: Nozzle diameter:* the diameter of the nozzle that you are going to use.

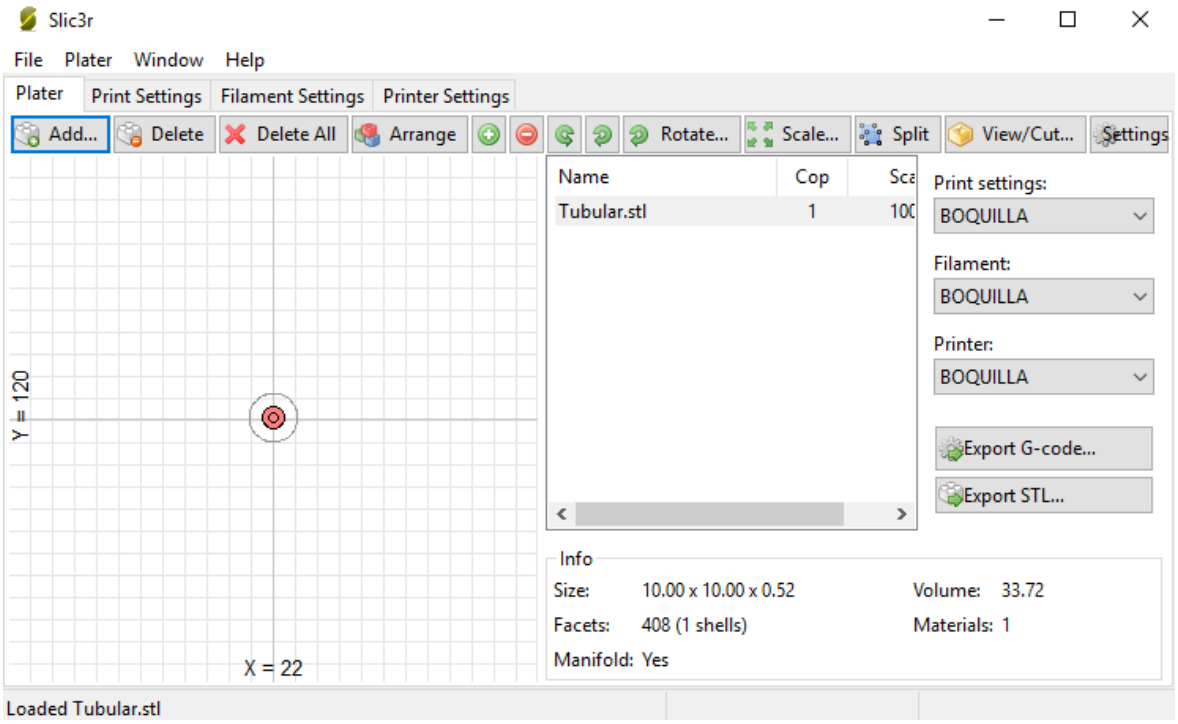

Figure B.1: *Main display of the software.*

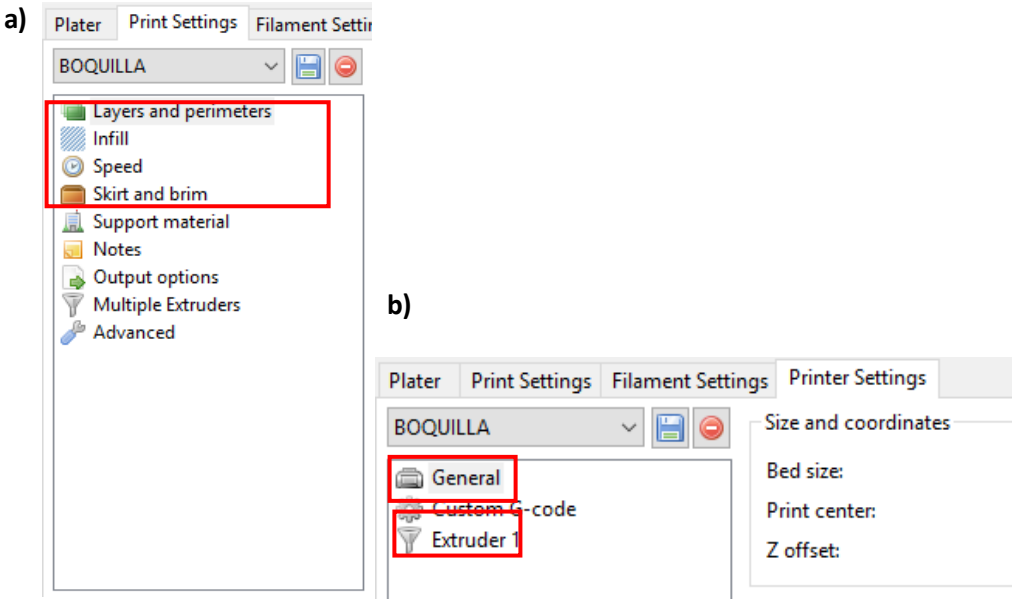

Figure B.2:*Both main menus of the principal paremetrs. a) Main menu of the* Print Settings. *b) Main menu of the* Printer Settings.

9.2.2. Annex B.2: ImageJ

Available: https://imagej.nih.gov/ij/, visited 30/05/2018

ImageJ is an image processing and analysis software written in Java, which allows it to run on Linux, Mac OS X and Windows, in both 32-bit and 64-bit modes. *ImageJ* and its Java source code are freely available and in the public domain. No license is required.

In this Bachelor's project this software is used to measure and for image processing in order to characterize the porosity of the samples.

In the following part, a brief explanation of these two applications will be presented.

A. Measure: This application is used to measure different parameters of an image.

1. Select the option to make lines in the picture (***Figure B.1 b***) and draw a line in the scale line push in *Ctrl+D.*
2. After that go to *Analyze (**Figure B.1 c**)* and chose *Set scale.* A new windows will be open (see ***Figure B.2 b***).
3. In the new windows the part of *Know distance*, goes the measure of the scale of the treated picture. Then in the part of *Unit of length*, goes the unit of the scale.
4. Finally with the option of drawing line (***Figure B.1 b***) you can draw lines and measure them push in *Ctrl+M,* and a new window is opened with all the measures.

B. Porosity: This application gives to you the option of measure the percentage of porosity of a picture and the measure of this porosity, making a black and white contrast of the picture.

1. Select the option *Image* (***Figure B.1 a***), then the option *Adjust (**Figure B.3 a**),* after that select *Treshold (**Figure B.3 b**)* and finally a windows is opened to modify the image (***Figure B.3 c***).
2. In the new windows opened (***Figure B.3 c***) you can modify the contrast as your desire to contrast the porosity just adjusting the above option, the green one. When you get the image as you want push the button *Apply.*
3. When the contrast image is generate, go to *Analyze (**Figure B.1 c**)* and chose the option *Analyze Particles* and a new window is opened.
4. In the new window with the defaulted options just choosing *Ok,* the programme generate two new windows; one of the percentage of the black pixels area that represents the porosity and the size of them. The other one is unusefull.

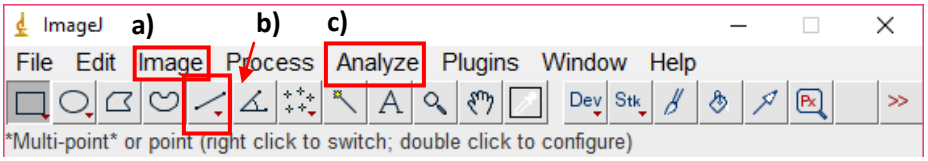

Figure B.1: *Principal menu of the* ImageJ *software.*

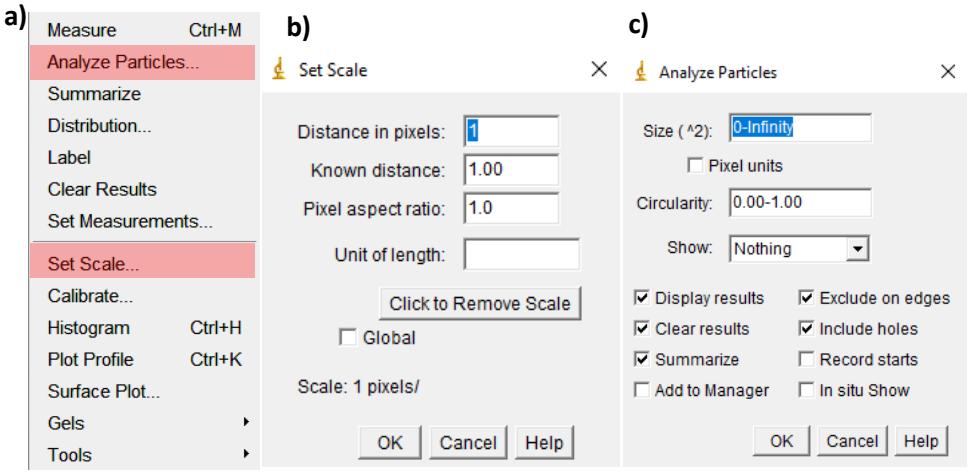

Figure B.2: *Analyze menu. a)Main analyze menu. b) Set scale window. c) Analyze particle window.*

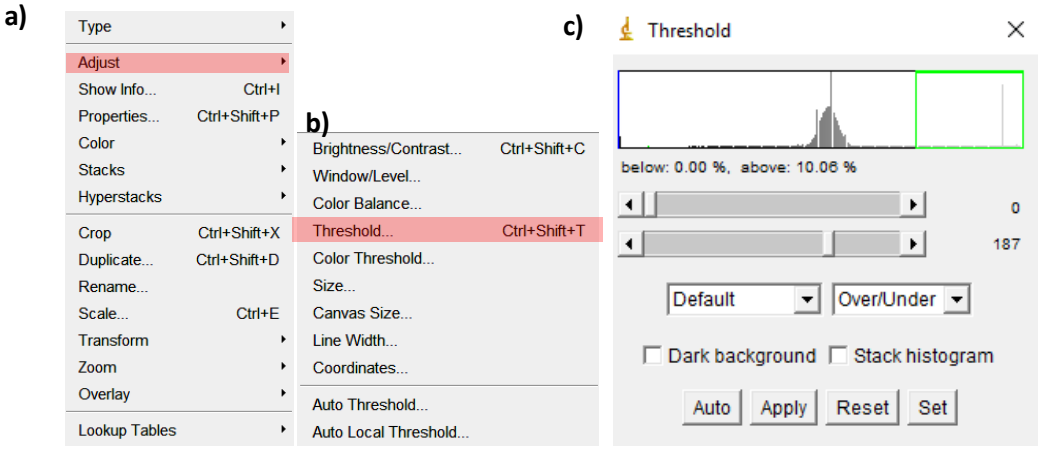

Figure B.3: *Image menu. a) Main image menu. b) Adjust menu. c) Treshold window.*

9.2.3. Annexe B.3: SolidWorks

SolidWorks is a 3D part design and modelling software, which the university pays the license. In this project this software is used to generate the layer to print. The principal tools that are used are the scratch to make the shape and the extruder tool to get a 3D figure with the high that the machine and the nozzle require. Finally the program gets to you a *STL.* file.

This file before of been read by the *Slic3r* software is needed to be processed by another program: *Netfabb.*

Netfabb:

Available: https://www.autodesk.com/education/free-software/netfabb, visited 28/05/2018.

Netfabb brings additive design and manufacturing tools together in a single software environment, giving product designers and engineers all the tools they need to optimize, validate and successfully produce models using additive manufacturing processes.

In this Bachelor's project this software is used to adjust and perform the *STL.* file before the *Slic3r* modification. The two main parameters are the centred of the figure and the correction of triangularization of the shape.